Fram Strait Marine Cold Air Outbreaks in CARRA and ERA5: Effects on Surface Turbulent Heat Fluxes and the Vertical Structure of the Troposphere

Nils Kristina Slättberg[1], Sandro Dahlke[2], and Marion Maturilli[2]

[1]Alfred Wegener Institute for Polar and Marine Research
[2]Alfred Wegener Institute, Helmholtz Centre for Polar and Marine Research

March 16, 2023

Abstract

Marine Cold Air Outbreaks (MCAOs) have a profound influence on atmospheric conditions and the surface-atmosphere heat exchange in Fram Strait and Svalbard. Comparing the global reanalysis ERA5 to its novel Arctic counterpart CARRA for November-March 1991-2020, we investigate the surface turbulent heat fluxes and the spatial characteristics of MCAOs throughout the troposphere. We find that the sensible heat flux from the surface to the atmosphere is substantially higher in CARRA, while the latent heat flux is higher in ERA5. For sensible heat flux, the differences scale with the magnitude, leading to maximum disagreement over the ice-free ocean where the flux is high. Accounting for the varying magnitude over different surface types, we find the largest relative disagreement over sea ice. During MCAOs, negative anomalies in temperature and specific humidity are present throughout the entire troposphere in both reanalyses. Meanwhile, positive heat flux anomalies are found in northwestern Fram Strait, where the sensible heat flux from the ocean to the atmosphere is roughly doubled during MCAOs. Around much of Svalbard, sea ice decline has caused positive trends in the surface-atmosphere potential temperature difference forming the basis of the MCAO index, leading to higher heat fluxes. In Fram Strait however, both reanalyses show negative trends in the MCAO index and the heat fluxes in January, when the increase in potential temperature is larger at 850 hPa than at the surface.

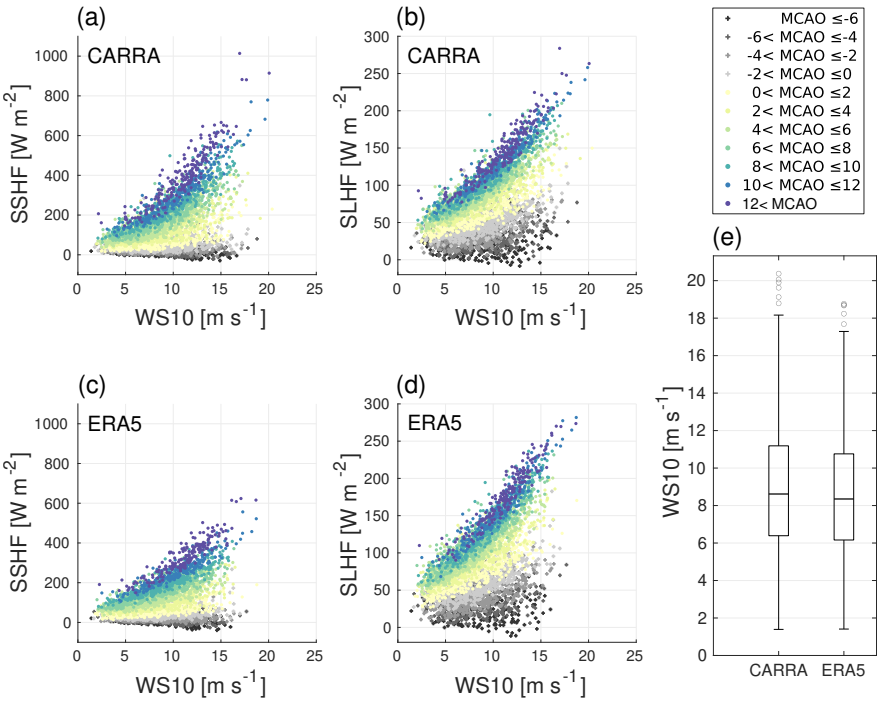

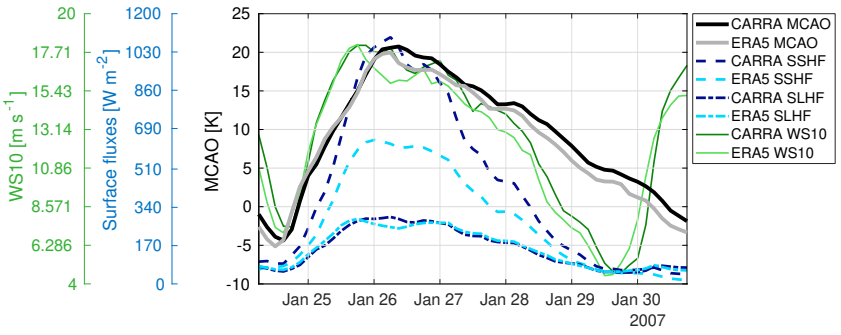

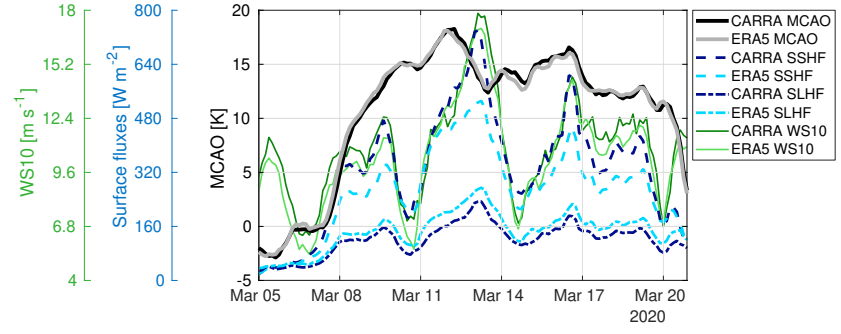

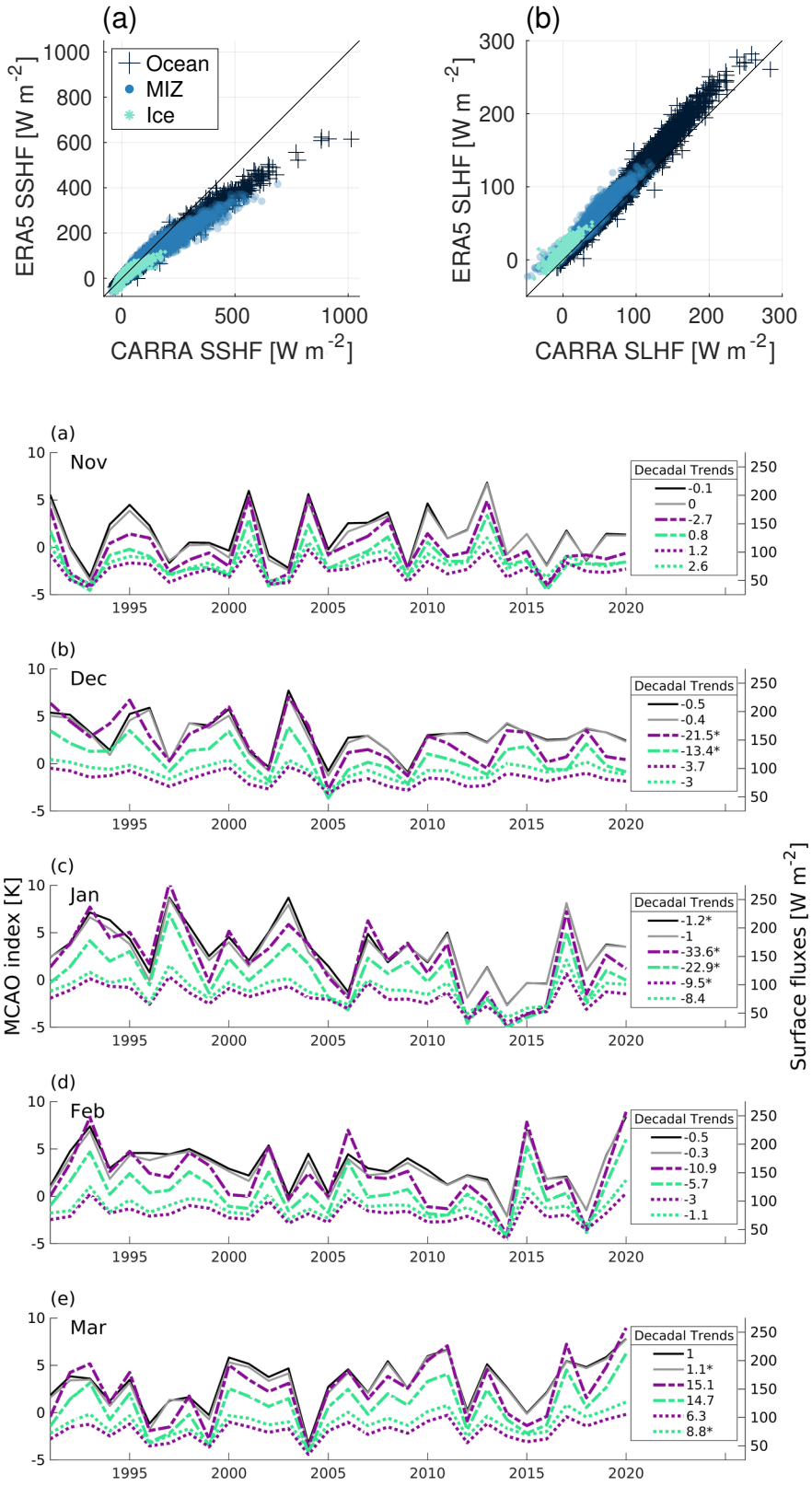

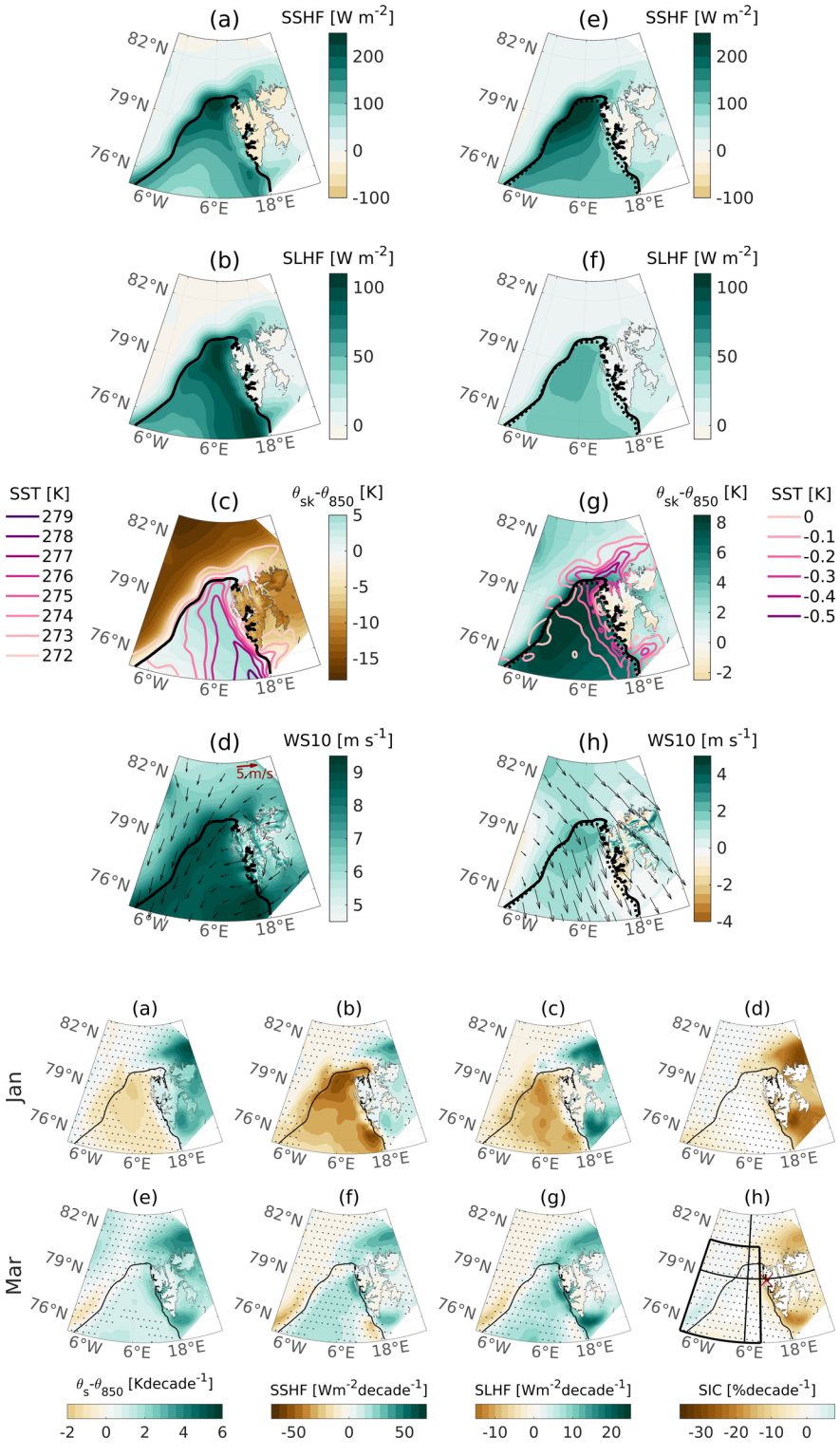

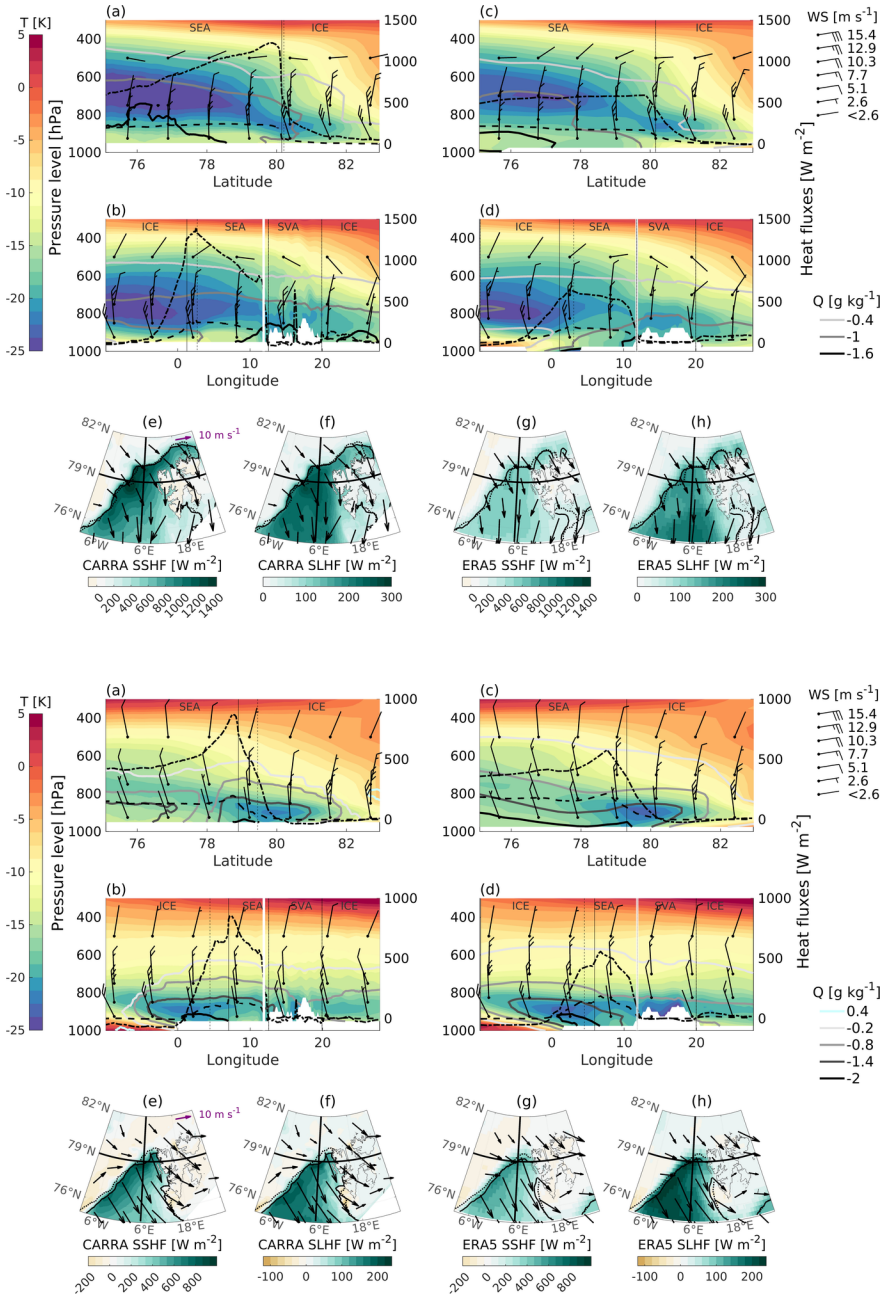

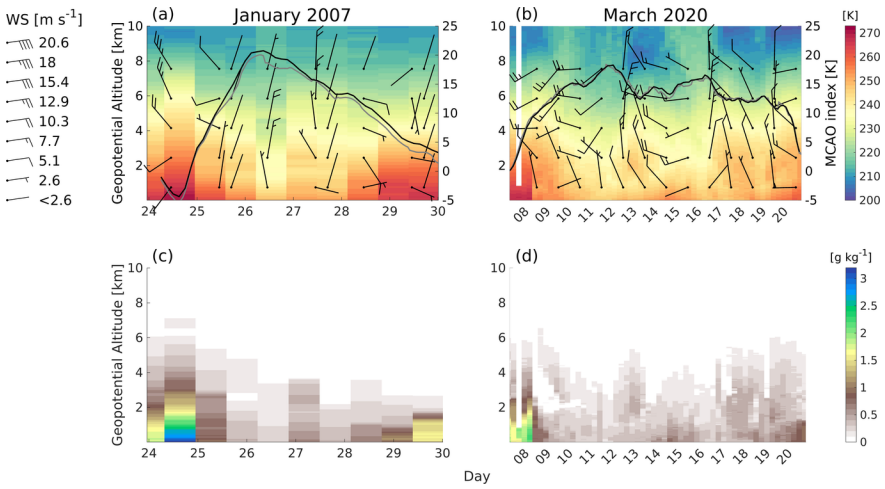

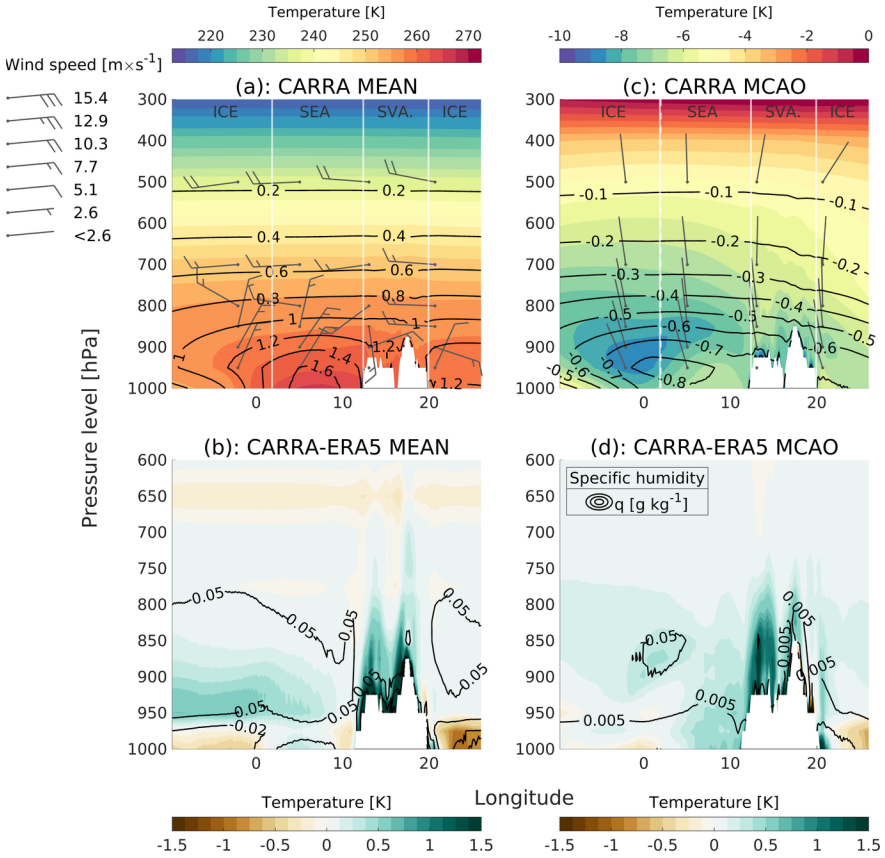

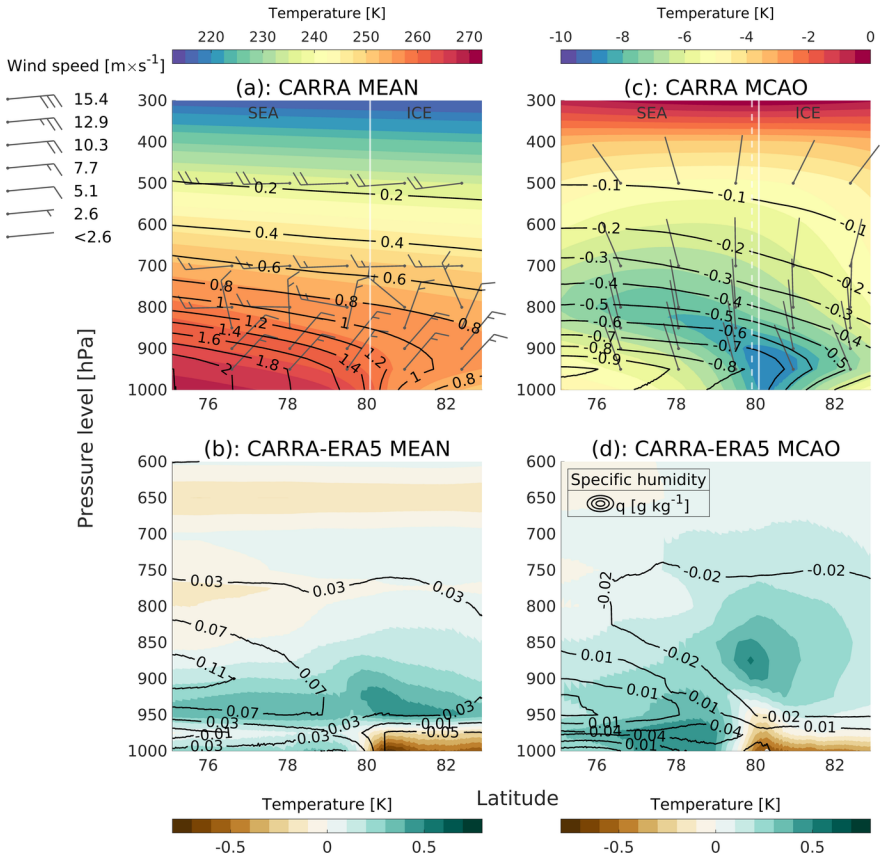

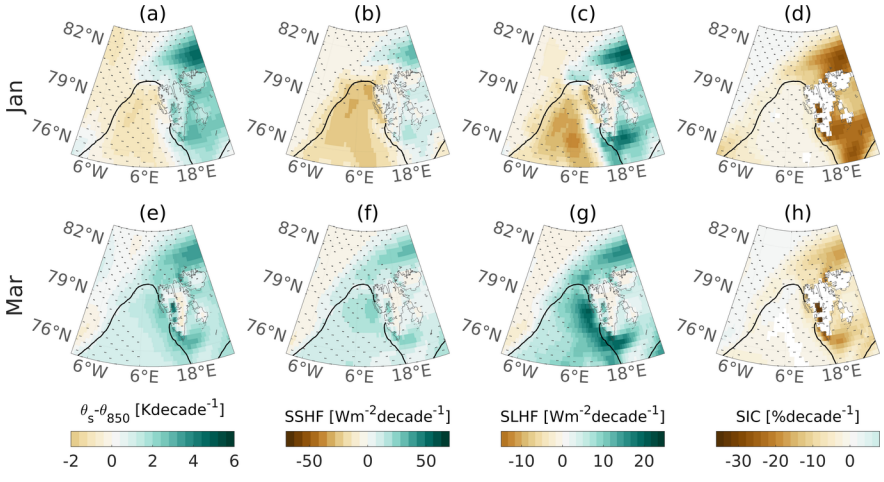

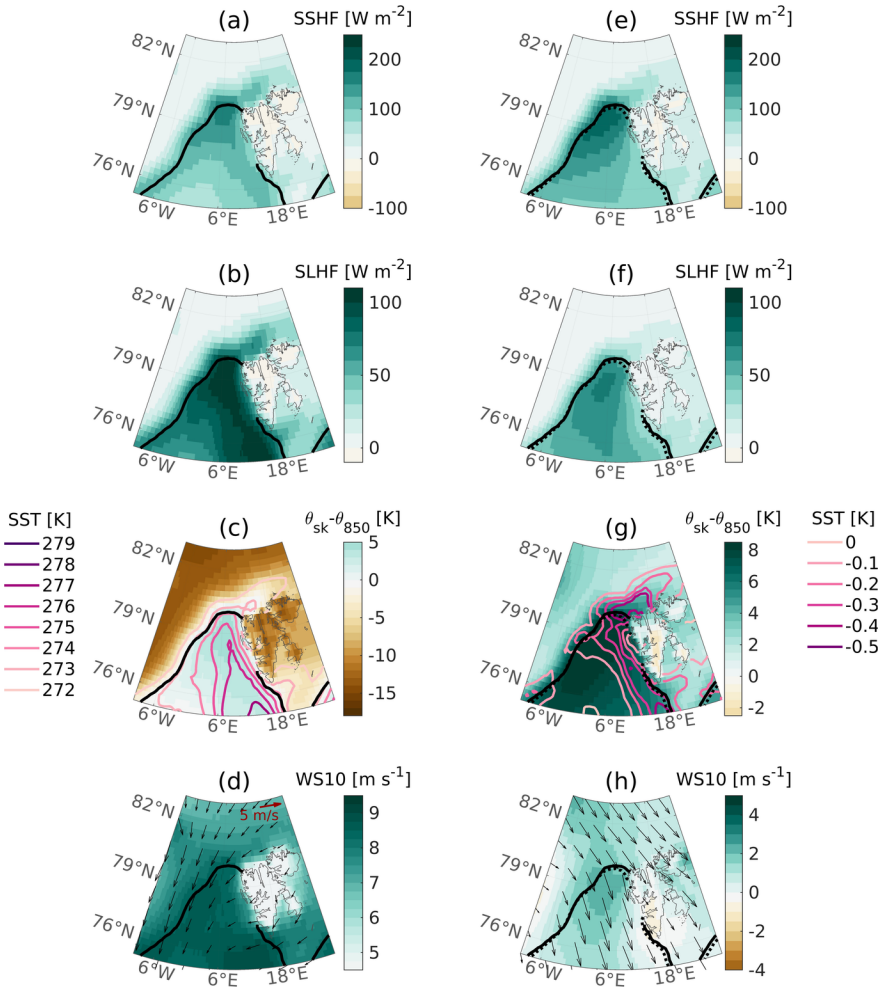

Fram Strait Marine Cold Air Outbreaks in CARRA and ERA5: Effects on Surface Turbulent Heat Fluxes and the Vertical Structure of the Troposphere

Nils Slättberg[1,2], Sandro Dahlke[1], Marion Maturilli[1]

[1]Alfred Wegener Institute Helmholtz Centre for Polar and Marine Research, Potsdam, Germany
[2]Leipzig University, Leipzig Institute for Meteorology, Leipzig, Germany

Key Points:

- Cold and dry anomalies are present throughout the troposphere during Fram Strait Marine Cold Air Outbreaks
- The surface sensible heat flux is substantially higher in CARRA than in ERA5 while the latent heat flux is lower
- The comparison indicates that known biases of ERA5 in the heat fluxes and the air temperature over sea ice and Svalbard are smaller in CARRA

Corresponding author: Nils Slättberg, `nils.slaettberg@awi.de`

Abstract

Marine Cold Air Outbreaks (MCAOs) have a profound influence on atmospheric conditions and the surface-atmosphere heat exchange in Fram Strait and Svalbard. Comparing the global reanalysis ERA5 to its novel Arctic counterpart CARRA for November-March 1991-2020, we investigate the surface turbulent heat fluxes and the spatial characteristics of MCAOs throughout the troposphere. We find that the sensible heat flux from the surface to the atmosphere is substantially higher in CARRA, while the latent heat flux is higher in ERA5. For sensible heat flux, the differences scale with the magnitude, leading to maximum disagreement over the ice-free ocean where the flux is high. Accounting for the varying magnitude over different surface types, we find the largest relative disagreement over sea ice. During MCAOs, negative anomalies in temperature and specific humidity are present throughout the entire troposphere in both reanalyses. Meanwhile, positive heat flux anomalies are found in northwestern Fram Strait, where the sensible heat flux from the ocean to the atmosphere is roughly doubled during MCAOs. Around much of Svalbard, sea ice decline has caused positive trends in the surface-atmosphere potential temperature difference forming the basis of the MCAO index, leading to higher heat fluxes. In Fram Strait however, both reanalyses show negative trends in the MCAO index and the heat fluxes in January, when the increase in potential temperature is larger at 850 hPa than at the surface.

Plain Language Summary

In Fram Strait, located between Greenland and Svalbard, Marine Cold Air Outbreaks (MCAOs) are formed when cold air moves from sea ice covered regions out over the open ocean. Because the air is so cold and dry compared to the ocean, vigorous heat transfer occurs in the form of sensible heat flux (heat from the ocean surface is transported to the air) and latent heat flux (water is evaporated). We compare the reanalysis datasets ERA5 and CARRA, and find that the sensible heat flux is much higher in CARRA, while the latent heat flux is somewhat higher in ERA5. We also find that during MCAOs, the entire troposphere (approximately the lowest 10 km of the atmosphere) becomes colder and drier. The heat fluxes are especially large in the northwestern part of ice-free Fram Strait during MCAOs, when the sensible heat flux in CARRA is twice as large as usual. Over the studied period, sea ice has decreased in much of the region, and therefore the heat fluxes have increased. In January however, the atmosphere warmed faster than the ocean surface, causing a smaller temperature difference between the surface and the air. Therefore, the heat fluxes in January have decreased.

1 Introduction

The Arctic climate and environment is transforming and particularly rapid changes are seen in the winter conditions of the Svalbard and Fram Strait region (Dahlke & Maturilli, 2017). In Fram Strait, the West Spitsbergen Current brings warm water northwards while the East Greenland Current carries cold Arctic water southwards (Rudels et al., 2012). Significant meridional transport occurs in the atmosphere as well, as cyclones and related intrusions of warm, moist air enters the Arctic from lower latitudes (Fearon et al., 2021). In the opposite direction, cold and dry Arctic air masses are advected in surges known as Marine Cold Air Outbreaks (MCAOs), which are very common in the Fram Strait during winter (Dahlke et al., 2022). Consequently, this region represents a major gateway of atmospheric (Tsukernik et al., 2007) and oceanic (Aagaard & Greisman, 1975) energy transports between the Arctic and lower latitudes, making it a hotspot for ocean–atmosphere energy exchanges (Wickström et al., 2020; Papritz & Spengler, 2017). Such exchanges include the turbulent heat fluxes, i.e surface sensible heat flux (SSHF) and surface latent heat flux (SLHF). These fluxes (collectively termed "heat fluxes" throughout this paper) exert a growing influence on Arctic climate vari-

ability as the temperature difference between the surface and the lower atmosphere changes in response to trends in sea ice characteristics (Taylor et al., 2018).

MCAOs are known to favor large heat fluxes in the Arctic (Papritz & Spengler, 2017). As cold air masses are advected over the relatively warm ocean surface they pick up heat and moisture, which leads to a rapid transformation of the air mass and can result in vigorous convection (Pithan et al., 2018). At the same time, the heat transfer cools the ocean mixed layer, facilitating dense water formation (Papritz & Spengler, 2017). In fact, MCAOs account for as much as 60-80% of the oceanic wintertime heat loss in the Nordic and Irminger Seas (Papritz & Spengler, 2017). MCAOs are thus of great importance for the transfer and distribution of heat within the highly coupled Arctic climate system.

Over Fram Strait, negative MCAO index trends in December and January were found in ERA5 for 1979-2020, when the difference between the potential temperature at the surface and 850 hPa was decreasing (Dahlke et al., 2022). For March, in contrast, Dahlke et al. (2022) identified a positive MCAO index trend, which was related to increased northerlies across Fram Strait. Given the strong effect of MCAOs on the heat fluxes, it is conceivable that they may change in response to the MCAO trends.

As noted above, MCAOs initiate convection, altering the vertical structure of the originally cold and dry air mass. MCAOs are thus associated with low static stability in the near surface air masses and typically result in organized convection, as often revealed by the formation of cloud streets or cellular cloud patterns (Brümmer & Pohlmann, 2000; E. W. Kolstad, 2011). Moreover, they often bring about severe weather and conditions suitable for the formation of intense mesoscale cyclones (Terpstra et al., 2021) such as polar lows (E. W. Kolstad, 2011). But how do the air mass properties change with height and how far beyond the surface do MCAOs extend? Airborne campaigns have allowed observations of the lower troposphere during specific MCAO cases (e.g. Knudsen et al. (2018), Michaelis et al. (2022), Hartmann et al. (1997)). In addition, Meyer et al. (2021) used a novel approach to investigate the 3-D structure of MCAO cases in the Barents and Nordic seas in ERA5. They point out that there is considerable variation in the shape and dynamics of different MCAOs. Therefore, we examine atmospheric properties associated with MCAOs on a climatological time scale. For this purpose, we use data from the global atmospheric reanalysis ERA5 (Hersbach et al., 2017, 2018, 2020) and its regional counterpart, the Copernicus Arctic Regional ReAnalysis (CARRA) (Schyberg et al., 2020). In addition, we provide detailed examination of two separate MCAO cases, for which we include radiosonde data from Ny-Ålesund, Svalbard.

Focusing on the Svalbard and Fram Strait region in November-March, when the prevalence of MCAOs is high, and limiting our study to 1991-2020, we investigate the following:

1. How does the novel CARRA reanalysis compare to ERA5 in terms of representing the heat fluxes and their relation with Fram Strait MCAOs?
2. What characterizes the vertical structure of the atmosphere during MCAOs and how does it vary over different surfaces and between CARRA and ERA5?

2 Data

We use three different data sources: ERA5 (Hersbach et al., 2017, 2018, 2020), CARRA (Schyberg et al., 2020), and radiosondes launched from Ny-Ålesund (Maturilli, 2008, 2020). In Ny-Ålesund, located on the west-coast of Svalbard (78.9°N, 11.9°E), radiosondes are launched daily at 12 UTC, with additional launches during specific campaigns. In our MCAO case study, we focus on two periods in January 2007 and March 2020, when radiosondes were launched twice per day (12 and 18 UTC) and four times per day (00, 06, 12 and 18 UTC), respectively.

Reanalysis assimilates observations into numerical weather prediction models to produce a physically consistent gridded dataset. However, reanalysis, especially in data-scarce regions like the Arctic, comes with uncertainties that may be hard to quantify.

Moreover, there can be substantial difference between reanalyses in the representation of the heat fluxes (Taylor et al., 2018). Investigating the surface meteorology and heat fluxes over the Iceland and Greenland Seas, Renfrew et al. (2021) found that although ERA5 performs well over open ocean, it is substantially less accurate in the marginal ice zone (MIZ). In addition, ERA5 overestimates the sea ice temperature (Batrak & Müller, 2019) and 2 m air temperature over sea ice (Wang et al., 2019), resulting in exaggerated long-wave flux (Graham, Cohen, et al., 2019). Still, unlike in-situ observations and satellite data, reanalysis provide the means to study spatiotemporal variability over several decades at a high spatial and temporal resolution. Moreover, ERA5 has been found to perform better than other reanalyses in the Fram Strait region (Graham, Hudson, & Maturilli, 2019). ERA5 has a horizontal resolution of 0.25° and is produced by the European Centre for Medium-range Weather Forecasts (ECMWF) within the Copernicus Climate Change Service. Data are available on an hourly time step and includes single level variables as well as data on 137 model levels or 37 pressure levels from 1000 hPa to 1 hPa.

CARRA was produced to reduce the above mentioned biases, mainly through enhanced treatment of cold surfaces (Yang et al., 2020), using a high horizontal resolution and assimilating more local observations (Køltzow et al., 2022). In a first evaluation, focusing on 2 m air temperature and WS10, Køltzow et al. (2022) found that CARRA indeed agrees better than ERA5 with observations. CARRA spans 1991-near present, has a horizontal resolution of 2.5 km and provides 3-hourly data for single levels as well as 23 pressure levels from 1000 hPa to 10 hPa. It is based on the HARMONIE-AROME numerical weather prediction system cycle 40h1.1 and receives its boundary conditions from ERA5 (Bengtsson et al., 2017; Køltzow et al., 2022). Data are provided for two regions in the North Atlantic Arctic. We use data from the western domain, which encompasses Greenland, Iceland and Svalbard. Details on how the heat fluxes were calculated in the reanalyses are given in the ECMWF documentation (ECMWF, 2016).

3 Methods

3.1 MCAO index

For each reanalysis, we calculated a daily (3-hourly for the case studies) MCAO index for the ice-free fraction of Fram Strait (defined here as 10°W-10°E, 75°N-81°N, see box in Figure 3 h), using the difference between potential skin temperature and potential temperature at the 850 hPa level as a proxy for MCAOs, following e.g. Dahlke et al. (2022). The MCAO index for each reanalysis was calculated at every horizontal grid-point and timestep as

$$MCAO_{idx} = \theta_s - \theta_{850}$$

where θ_s and θ_{850} are the daily mean potential skin temperature and the daily mean potential temperature at 850 hPa, respectively. Thereafter, grid cells with sea ice concentration (SIC) $> 15\%$ were excluded before calculating the mean over Fram Strait. Where spatially averaged WS10 and heat fluxes were analyzed together with the MCAO index, these were averaged over the same grid points for comparability.

3.2 Statistical methods and data treatment

We analyzed data for the extended winter (November-March), from 1991 to 2020, for the Svalbard and Fram Strait region (10°W-28°E, 75°N-83°N). We used linear regression for computing trends over time and relationships between variables, and Pearson's R for correlation, in both cases with 95% as confidence level. In addition, we calculated the Root Mean Squared Error (RMSE) between the heat fluxes in CARRA and ERA5 and normalized it by the interquartile range of the heat flux in CARRA over ocean, the MIZ, and sea ice, respectively. Following the recommendation in the user guide, the spin-up period (first 6 hours of each run) was removed from the CARRA heat fluxes (Nielsen,

K. P. and Yang, X. and Agersten, S. and Dahlgren, P. and Ødegaard Køltzow, M. A. and Schyberg, H. and Støylen, E. and Bojarova, J., 2022). Throughout this paper, positive values denote a heat flux from the surface to the atmosphere. We define ice-free ocean as SIC $<$ 15%, MIZ as SIC = 15-80%, and sea ice as SIC $>$ 80% (Strong et al., 2017).

Before investigating the respective influences of the MCAO index and the 10 m wind speed (WS10) by correlating each of them with the heat fluxes, the correlation between the two predictors was removed. This was achieved by computing the regression slope b for the MCAO index vs WS10 and thereafter subtracting $b\times$WS10 from the MCAO index, and vice versa. Moreover, we performed linear regression between each of the two predictors and the heat fluxes and multiplied the regression coefficient with the standard deviation of each predictor to make their influences comparable. When averaging WS10 over time, we calculated scalar averages (the wind speed was calculated from the u and v components *before* averaging over time) except for the wind arrows. Instead, the length of the wind arrows correspond to the vector average wind speed (the u and v components were averaged over time and the wind speed computed from these averages), since wind direction also must be taken into consideration when drawing the arrows.

3.3 MCAO threshold and composite analysis

MCAOs are often classified using one or several threshold values of the θ_S-θ_{850} difference. Since the Fram Strait region is prone to intense (θ_S-θ_{850} $>$ 8 K) MCAOs (Papritz & Spengler, 2017), we chose 8 K. This threshold corresponds to the 81st (83rd) percentile in CARRA (ERA5), and ensures that a sufficient number of observations (at least 96 (91) in CARRA (ERA5)) are included in the composite for each month. Applying other thresholds yielded qualitatively similar results, indicating that the results are not particularly sensitive to the choice of threshold. Composites showing the mean conditions were computed as the mean of a meteorological variable x for all days in month m. Similarly, the MCAO composites are the mean of x for all days in month m with the MCAO index $>$ 8 K. The monthly composites were then averaged to produce a mean for the entire extended winter, and the MCAO anomalies were computed from these averaged composites as $x_{MCAO}-x_{mean}$. Composites were computed for surface variables as well as the atmospheric cross sections described below.

3.4 Atmospheric cross sections

To investigate the vertical structure of the troposphere during MCAOs, we extracted one cross section at 6°E from 75°N to 83°N, and one at 79°N from 10°W to 26°E. The former exclusively covers sea ice and ocean, while the latter also encompasses Svalbard land regions, including Ny-Ålesund, the radiosonde launch site for the case studies. Data on pressure levels with higher pressure than the surface were removed to avoid presenting data for non-existing pressure levels. To analyze the CARRA-ERA5 differences, we linearly interpolated the cross sections to the same axes using the nearest two grid points and subtracted the ERA5 data from the CARRA data. Since CARRA (ERA5) has a lower vertical (horizontal) resolution, the CARRA cross sections were interpolated to the vertical levels of ERA5, and the ERA5 cross sections to the horizontal coordinates of CARRA.

4 Fram Strait heat fluxes in CARRA and ERA5

We compute the correlation between the daily Fram Strait MCAO indices from CARRA and ERA5 and find significant correlations with the coefficient R $\geq$0.99 in each of the investigated months. The CARRA MCAO index has a higher mean (2.8 K) than ERA5 (2.5 K), with bigger differences in the first half of the period, as visible in the monthly mean time series (Figure A1). The daily mean heat fluxes (averaged over ice-free Fram Strait) are significantly correlated, with R $\geq$0.98 and R $\geq$0.99 for SSHF and SLHF, re-

spectively. However, as we will see in the following sections, there is substantial disagreement between the two reanalyses regarding the *magnitude* of the heat fluxes.

ERA5 has previously been evaluated against a meteorological buoy in the Iceland Sea (Renfrew et al., 2021). While its performance was better there than in the MIZ, ERA5 overestimated the SLHF and slightly underestimated the SSHF, although the bias was not statistically significant for the latter (see Figure 3 e-f and Table 2 in Renfrew et al. (2021). More broadly, ERA5 has also been found to overestimate the SLHF over the global land surface (Martens et al., 2020). The differences between the two reanalyses could therefore result from improvements in CARRA, since it tends to have larger SSHF and smaller SLHF than ERA5, as indicated by Figure 1. In this case, the largest differences should perhaps be found over the MIZ, where ERA5 performs poorly (Renfrew et al., 2021), or over sea ice, since CARRA uses a more sophisticated representation of sea ice and snow on sea ice. In addition, CARRA has previously been found to show large differences (in 2 m air temperature) from ERA5 over sea ice in winter (Køltzow et al., 2022). To assess the size of the CARRA-ERA5 differences in relation to the magnitude of the heat flux over each surface type, we calculate the normalized RMSE (see Section 3). For SSHF, we find normalized RMSEs of 0.30 Wm^{-2} over the ocean as well as the MIZ. Over sea ice, the disagreement is more than twice as high (0.69 Wm^{-2}). The corresponding numbers for SLHF are 0.28 Wm^{-2} over ocean, 0.50 Wm^{-2} over the MIZ, and 2.11 Wm^{-2} over sea ice. Thus, while the largest absolute differences between CARRA and ERA5 are found in SSHF over the ocean, the normalized difference is largest over ice, and is particularly large for SLHF. Although evaluation against independent observations are needed to confirm it, this indicates that heat flux biases over sea ice may indeed be reduced in CARRA.

4.1 The relative influences of wind speed and the MCAO index

MCAOs can extract heat and moisture from the ocean by introducing large surface-atmosphere differences in temperature and humidity. In addition to these vertical gradients, the heat fluxes are affected by wind speed. In the following, we investigate the relative influences of the MCAO index and WS10 on the heat fluxes in ice-free Fram Strait. Since the wind speed is often higher than average during strong MCAOs (E. Kolstad, 2017), the WS10 and the MCAO index may not be independent from each other. Therefore, we removed the correlation between these two predictors before correlating each of them with the heat fluxes (see Section 3 for details).

As evident from Figure 2, the relationship between WS10 and the fluxes is highly dependent on the MCAO index in both reanalyses. While virtually no relationship is apparent during negative MCAO index, higher values correspond to increasingly stronger WS10-flux relationship. The largest heat fluxes are found when both the WS10 and the MCAO index are high, i.e. when high wind speeds occur along with unstable stratification. For both fluxes, the correlation with WS10 is lower than the correlation with the MCAO index, which shows explained variances (R^2) of at least 0.5 in both reanalyses, indicating that at least 50% of the variability in the heat fluxes can be explained by the MCAO index (Table 1). Comparing the normalized regression coefficients, we find that the variations in the MCAO index correspond to a larger amount of change in the fluxes than the variations in WS10. This is in line with Taylor et al. (2018), who tested the sensitivities of satellite-derived heat fluxes to wind speed and the vertical temperature and humidity gradients between the surface and the atmosphere. They found that SSHF (SLHF) is dominated by the vertical temperature (humidity) gradient, while wind speed plays a smaller role. However, Figure 2 demonstrates that WS10 has a substantial impact in the case of strong MCAO events, during which fluxes concurring with high wind speed are typically at least twice as high as when the wind speed is low.

As for the CARRA-ERA5 differences, the higher SSHF in CARRA may partly be related to the somewhat higher MCAO index (Figure A1). In addition, the maximum WS10 is higher in CARRA (Figure 2 e), which has previously been found to outperform

ERA5 in the representation of wind speed (Køltzow et al., 2022). It is thus possible that improved WS10 along with higher MCAO index values contributes to the higher SSHF in CARRA. However, higher SSHF can be seen also for a given WS10 and MCAO class, indicating that the magnitude of the influence of each predictor also plays a role. Comparing the normalized regression coefficients, we find that both WS10 and the MCAO index correspond to a larger SSHF change in CARRA than in ERA5 (Table 1). The higher SSHF in CARRA can thereby be explained as the combined result of higher MCAO index, higher wind speed, and a stronger response of the SSHF to both of these. For SLHF in contrast, both predictors are associated with a larger change in ERA5. In addition, the surface-atmosphere humidity gradient, which was not investigated here, may differ between the reanalyses.

Table 1. Coefficients from correlations (R) and regressions (b) of the daily Marine Cold Air Outbreak (MCAO) index and 10 m wind speed (WS10), respectively, with the surface fluxes. Shown is also the normalized regression coefficients (b multiplied with the standard deviation of each predictor; STD_M for MCAO and STD_W for WS10). Values for CARRA are followed by values for ERA5 in brackets. All correlations and regressions are statistically significant at the 95% level.

Variables	**R**	$\mathbf{R^2}$	**b** $[\mathbf{Wm^{-2}K^{-1}}]$	$\mathbf{bSTD}_M$ $[\mathbf{Wm^{-2}}]$
MCAO vs SSHF	0.72 (0.77)	0.51 (0.59)	18 (15)	97 (78)
MCAO vs SLHF	0.71 (0.72)	0.50 (0.52)	6 (7)	33 (39)
Variables	**R**	$\mathbf{R^2}$	**b** $[\mathbf{Wm^{-2}(ms^{-1})^{-1}}]$	$\mathbf{bSTD}_W$ $[\mathbf{Wm^{-2}}]$
WS10 vs SSHF	0.40 (0.33)	0.16 (0.11)	20 (14)	63 (44)
WS10 vs SLHF	0.48 (0.45)	0.23 (0.20)	8 (9)	24 (27)

5 Spatial patterns

5.1 Heat flux trends in conjunction with MCAO and sea ice changes

To better understand how the heat fluxes may change in response to MCAO changes, we examine the spatial patterns of the trends in monthly mean heat fluxes and θ_S-θ_{850} (spatially averaged trends for ice-free Fram Strait are displayed in Figure A1). Since the fluxes are heavily impacted by sea ice distribution (Taylor et al., 2018), we also include the SIC trends. ERA5 and CARRA mainly shows similar patterns so ERA5 is excluded from the following discussion, but its trends are displayed in Figure A2. Since the direction of some of the trends change between months, we do not average over the extended winter. Instead, we choose January and March, which show opposing trends in the θ_S-θ_{850} difference as well as the heat fluxes. While March is the only month for which positive flux and θ_S-θ_{850} trends are found in Fram Strait, the trend patterns in January resemble those found in November, December and February, but are more pronounced and exhibit significance over a wider area.

Negative θ_S-θ_{850} and heat flux trends prevail in Fram Strait in January (Figure 3 a-c). The negative θ_S-θ_{850} trends are a result of the θ_{850} rising faster than the θ_s (not shown). Meanwhile, pronounced positive trends are seen north, east and south of Svalbard, corresponding to areas of declining sea ice (Figure 3 d). Arctic heat flux trends have been investigated by Boisvert et al. (2022), who computed satellite-derived winter trends for the 2002-2020 period. While not directly comparable due to the different periods and averaging, it can be noted that they found negative trends in southeastern Fram Strait and near-zero or weakly positive trends over the sea ice (see their Figure 3 g & h). Their negative heat flux trends are considerably weaker and there appears to be a

stronger tendency towards positive trends, at least in the SSHF over the sea ice and along the west coast of Svalbard.

March exhibits positive θ_S-θ_{850} and heat flux trends around Svalbard, mirroring the negative trends in SIC (Figure 3 e-h). As noted above, the θ_S-θ_{850} and heat flux trends in the ice-free Fram Strait are also positive, although statistical significance is largely lacking, especially for SSHF. The spatial pattern of the SLHF trend closely resembles that of θ_S-θ_{850}, indicating that the latter may shape the spatial distribution of the SLHF trends. The θ_S-θ_{850} trends, in turn, are not just the result of increasing θ_s but also of decreasing θ_{850} (not shown), consistent with the circulation change promoting northerlies in March, as noted by Dahlke et al. (2022). A negative temperature trend around the height of the 850 hPa level in March is also seen in the homogenized radiosonde record from Ny-Ålesund (Maturilli & Kayser, 2017). South of the climatological ice edge, the SIC is zero throughout the period in most of Fram Strait. However, negative SIC trends in the south-westernmost part of the study area and along the Svalbard west coast likely contribute to the positive θ_S-θ_{850} and heat flux trends in these regions.

5.2 Surface meteorology during MCAOs

We investigate the heat fluxes, WS10, 10 m wind direction, and θ_S-θ_{850} as composites for the extended winter mean and MCAO anomalies (MCAO-mean) in Figure 4. For brevity, only CARRA is discussed here, but a corresponding figure for ERA5 is provided in the supplement (Figure A3). The mean SSHF in CARRA is largest in the northernmost part of the ice-free Fram Strait, where it approaches 250 W m^{-2}, and near zero or negative over the sea ice and Svalbard (Figure 4 a). The spatial pattern can be explained by a combination of the distributions of θ_S-θ_{850} and WS10 (Figure 4 c and d): High SSHF extend from the ice edge in the north along the eastern side of Fram Strait (where θ_S-θ_{850} is relatively high) as well as the western (where WS10 is relatively high). Positive SSHF is also present in the Whalers Bay Polynya region north of Svalbard, likely reflecting areas of relatively small SIC (not shown) and a local maximum in WS10. In contrast, the low SSHF over the sea ice and Svalbard corresponds to negative θ_S-θ_{850} and low WS10. The MCAO anomalies in SSHF are of similar magnitude as the mean SSHF, and exhibit their largest values in the northwestern part of ice-free Fram Strait, which is also where the anomalies in θ_S-θ_{850} and WS10 are the largest (Figure 4 e, g and h).

The mean SLHF is near zero or weakly negative over the sea ice and Svalbard. In ice-free Fram Strait, it reaches up to 110 W m^{-2} in the east and decreases westward, somewhat resembling the sea surface temperature (SST), with high values along the warm West Spitsbergen Current (Figure 4 b and contour lines in c). We speculate that the apparent dependence of SLHF on SST may be related to higher near-surface temperatures over warm ocean raising the saturation water vapor pressure and thereby promoting large SLHF, as described in Hartmann et al. (1997). Similar to SSHF, the MCAO anomalies in SLHF, which reach up to almost 60 W m^{-2}, are centered in the northwestern part of ice-free Fram Strait, where the anomalies in θ_S-θ_{850} and WS10 are large (Figure 4 f).

The mean θ_S-θ_{850} reflects the distribution of sea ice, land, and SST variability (Figure 4 c). The MCAO anomalies in θ_S-θ_{850} are strongest in the western part of ice-free Fram Strait, where cold air is advected over the ice edge (Figure 4 g). In this region, the temperature at 850 hPa is 8 K lower than during mean conditions while the skin temperature hardly exhibits any anomalies (not shown), demonstrating that the large θ_S-θ_{850} difference during MCAOs results from changes in air temperature rather than surface temperature. This is in line with E. W. Kolstad et al. (2009), who found that atmospheric temperature variations are more important than SST variations for MCAO variability in the northern North Atlantic. The SST anomalies are weak and predominantly negative, with the largest negative values along the West Spitsbergen current and in the Whalers Bay Polynya region. The prevalence of negative SST anomalies during MCAOs is perhaps surprising, since lower temperature at the surface acts to decrease

the vertical temperature gradient. Moreover, a positive relation between SST and Barents Sea MCAOs was found in Polkova et al. (2021). However, the relation with the SST may differ between regions and MCAO strengths. The negative SST anomalies in Figure 4 g likely result from positive SIC anomalies (not shown) and from the MCAO air masses cooling the ocean surface.

MCAO anomalies of up to 5.5 m s^{-1} are seen in the wind speed, while the wind direction is more northwesterly than during mean conditions (Figure 4 h). Smaller regions of negative WS10 anomalies are seen in the westernmost part of the study area and over parts of Svalbard. It is likely that the negative WS10 anomalies in the former region arise due to high pressure over Greenland, which is associated with the larger-scale pressure pattern that is typical for Fram Strait MCAOs (Dahlke et al., 2022). The negative WS10 anomalies over Svalbard may result from topography, as the wind direction near the surface is altered in regions that are sheltered from the synoptic flow by topographic barriers. In conclusion, the typical MCAO fingerprint in this region includes anomalously strong and northwesterly 10 m winds, acting together with the large θ_S-θ_{850} difference to produce high heat fluxes. The θ_S-θ_{850} and heat flux anomalies are particularly strong in the northwestern part of ice-free Fram Strait, where the cold air masses are being advected over the ice edge.

5.3 Atmospheric conditions during MCAOs

To explore the vertical characteristics of MCAOs, we analyze CARRA and CARRA-ERA5 cross sections at 6°E and 79°N (lines in Figure 3 h). CARRA is shown from the surface to 300 hPa (approximately the height of the tropopause), while levels above 600 hPa are omitted in the difference plots to better demonstrate near-surface patterns (differences at higher levels are small and mainly concentrated at pressure levels that are absent in CARRA and therefore contains interpolated data). Non-negligible differences in wind speed and direction are confined to small regions that are not well represented by wind barbs, which are also omitted in the difference plots.

In the lower layers, the extended winter mean temperature along the cross section at 6°E ranges from 273 K over the ocean in the south to 252 K above the sea ice in the north, where a temperature inversion is present (Figure 5 a). In the upper layers, the influence of the surface is weaker and the latitudinal temperature difference smaller. The humidity distribution resembles the temperature distribution, with the highest values (2 g kg^{-1}) near the surface in the south. From 700 hPa and aloft, westerly winds prevail, while the lower atmosphere is dominated by northeasterly winds. The largest CARRA-ERA5 temperature difference is found in a shallow layer above the sea ice north of 80°N, where ERA5 is almost 0.8 K warmer and has up to 0.07 g kg^{-1} higher specific humidity (Figure 5 b). The magnitude of the temperature difference is similar to Køltzow et al. (2022), who found an absolute difference between CARRA and ERA5 of 0.5-1 K over the sea ice north of Svalbard. The lower temperature in CARRA is a promising sign that the temperature overestimation in ERA5 over sea ice (Batrak & Müller, 2019; Wang et al., 2019) may be reduced in CARRA. Just above the surface layer, ERA5 is instead somewhat colder than CARRA, especially in the vicinity of the ice edge, where the difference reaches 0.5 K.

During MCAO conditions, the wind shows anomalies with a northerly component throughout the troposphere (Figure 5 c). The temperature and humidity is decreased everywhere, but the distributions of their anomalies differ. For specific humidity, the MCAO conditions manifest most strongly above the ice-free ocean in the south, where the anomalies exceeds -1 g kg^{-1}. At higher altitudes and over the sea ice, the anomalies are smaller since these regions are relatively dry in the mean conditions as well. The temperature anomalies are largest near the ice edge, reaching -9 K in CARRA. Over the ocean, the altitude of the strongest anomalies increases with the distance from the ice edge. This can be explained by the progressive warming of the air by the heat fluxes, transforming the air mass and eventually destroying the MCAO. North of the ice edge, the anomaly

decreases with increasing latitude, since the air over the ice is relatively cold also in the mean state. The temperature is higher in CARRA than in ERA5 throughout most of the cross section, but the warmer layer in ERA5 over the sea ice is still present (Figure 5 d). Around 850 hPa, over the ice edge, the temperature is 0.5 K higher in CARRA, but the specific humidity somewhat lower (0.05 g kg^{-1}). At the 975 hPa level, which is absent in CARRA, the CARRA-ERA5 difference reaches 0.06 g kg^{-1}, indicating that the representation of near-surface humidity is impacted by the exclusion of the 975 hPa level in CARRA.

Along the cross section at 79°N, the extended winter mean temperature in CARRA is highest (265.5 K) over the ice-free ocean and lowest (254.5 K) over the sea ice in the west (Figure 6 a). The specific humidity distribution follows the same pattern, and has its maximum (1.6 g kg^{-1}) over the ice-free ocean. The largest CARRA-ERA5 difference is seen over the land surface of Svalbard, where the temperature (specific humidity) is up to 4.5 K (0.4 g kg^{-1}) higher in CARRA (Figure 6 b). For comparison, Køltzow et al. (2022) found that ERA5 underestimates the (2 m) temperature over Svalbard with biases of around -1.5 K in winter, while CARRA shows a much smaller overestimation.

Strong MCAO anomalies in temperature are found in two distinct regions (Figure 6 c). One of these is situated near the ice edge close to 0°E, where anomalies reaching -8 K are centered around the 900-950 hPa altitude. The strongest anomalies, however, reach -10 K in CARRA and are found close to the land surface of Svalbard. This is also where the CARRA-ERA5 differences are the largest, with ERA5 displaying anomalies that are up to 2.8 K colder (Figure 6 d). While ERA5 is generally colder, the strength and even the sign of the differences changes between individual grid cells over the topography of Svalbard, indicating that the difference between the reanalyses is impacted by the lower horizontal resolution of ERA5. The largest MCAO anomalies in humidity (around -1 g kg^{-1} in CARRA) are found over ice-free ocean in Fram Strait. In the lower levels, the near surface specific humidity is higher in CARRA, especially over the sea ice east of Svalbard. Around 900 hPa, where large MCAO anomalies in temperature are found, the specific humidity is instead lower in CARRA.

6 A comparison of two MCAO cases

We identify two MCAOs cases, which are very different in terms of the temporal evolution and duration of the MCAO and its effects on atmospheric anomalies and heat flux variability. These cases coincide with extra radiosonde launches from Ny-Ålesund, allowing for a detailed examination of the vertical extent. The first case includes the highest value found in our daily mean MCAO indices (19.9 K in CARRA, 18.5 K in ERA5), while the second case exemplifies a slightly weaker but more prolonged case, during which the heat flux variability appears to be dominated by WS10.

6.1 January 2007

The first case takes place 25-28 January 2007 and displays a rapid increase in the 3-hourly MCAO indices from about 5 K to 20 K during the first day of the event, followed by a roughly linear decline over the next few days (Figure 7). The MCAO indices and SSHF peak on the 26th, which is also when the SSHF difference is the largest, with CARRA exceeding 1000 Wm^{-2} and ERA5 reaching just over 600 Wm^{-2}. The SLHF, also peaking around the 26th, is similar in both datasets and exhibits a much smaller range, with pre-event values similar to those of SSHF but peak values barely reaching 300 Wm^{-2}. The WS10 is highest (18 ms^{-1}) on the 25th, and tends to be somewhat higher in CARRA.

To extract MCAO anomalies in temperature, wind and specific humidity, the daily mean conditions on the 24th were subtracted from the daily mean conditions on the 26th. The resulting MCAO anomalies are shown for the cross sections at 6°E and 79°N, for CARRA

(Figure 8 a-b) and ERA5 (Figure 8 c-d). The corresponding anomalies in the heat fluxes and wind at 10 m are shown in Figure 8 e-h.

The most pronounced cold anomalies exceed 24 K in both reanalyses, although the areas of strong cooling are larger in CARRA. Along the cross section at 6°E, the strongest cold anomalies are found over the ocean around 600-750 hPa. Over ice, the anomalies are somewhat more confined to the surface layers, consistent with Figures 5 and 6. At 79°N however, the cold anomalies over the sea ice in western Fram Strait display a similar detachment from the near surface layers, with the maximum cooling centered on 750 hPa.

For specific humidity, the largest anomalies reach -2.6 g kg^{-1} in CARRA (-2 g kg^{-1} in ERA5) and are found over the ocean in the southern part of the 6°E cross section. Along 79°N, the largest humidity anomalies are found near Svalbard and, particularly in ERA5, over the Fram Strait.

The wind anomalies at 10 meters are mainly northwesterly over the sea ice and central Fram Strait (Figure 8 e-h). In the vertical, wind anomalies below 600 hPa are mainly northerly, while anomalies with easterly components are found in the upper layers (Figure 8 a-d). The wind speed anomalies are generally below 2.6 m s^{-1}, but anomalies exceeding 15 m s^{-1} are found over the ice in the north and west at around 800-900 hPa. There is a tendency towards stronger wind speed anomalies in CARRA, for instance over Svalbard.

The SSHF anomalies, which reach 1400 (640) Wm^{-2} in CARRA (ERA5), are largest along the ice edge in Fram Strait and weakens gradually towards southeast (Figure 8 e & g). The strong anomalies near the ice edge are also evident in the cross sections, where SSHF near the ice edge reaches well over 1000 Wm^{-2} in CARRA and around 600 in ERA5 (Figure 8 a-d).

For the SLHF, there is a clear difference between the two reanalyses in the spatial distribution of the anomalies (Figure 8 f & h). While CARRA displays SLHF anomalies that are largest (Wm^{-2}) in northwestern Fram Strait and decrease with distance from the ice edge, ERA5 shows its largest SLHF anomaly (230 Wm^{-2}) in southern Fram Strait. This difference can also be seen along the north-south cross section, where the SLHF in ERA5, unlike CARRA, increases towards the south (Figure 8 a & c). Theoretically, SLHF that increases with distance from the ice edge could be explained by a gradual increase in near-surface temperature, as seen in (Hartmann et al., 1997). Higher temperature further away from the ice edge would act to raise the saturation water vapor pressure and thereby the SLHF, while dampening the SSHF by reducing the vertical temperature gradient. The southwards increase in the SLHF may therefore potentially be related to the gradual southwards temperature increase south of 79°N, which is seen in the low level temperatures of ERA5 (Figure 8 c) but not CARRA (Figure 8 a).

6.2 March 2020

In the March 2020 case, the MCAO index remains above 8 K from 8th to 20th March 2020 (Figure 9). The MCAO indices as well as the fluxes oscillate between higher and lower values during the event, but there is no obvious agreement between their fluctuations. The WS10 in contrast shows a clear co-variability with the fluxes in both reanalyses, suggesting that it dominates their variability during the event. This agrees with our findings in Section 4.1, demonstrating that WS10 is strongly related to the fluxes during MCAOs.

For the March case, the daily mean conditions on the 12th was subtracted from the daily mean conditions on the 5th to produce the MCAO anomalies (Figure 10. Roughly northerly wind anomalies are present throughout the troposphere along with cold anomalies, which are mainly found near the surface over land and ice, and at 700-800 hPa over the ocean. However, the strongest temperature anomalies are weaker and more confined to the surface than in the January case, perhaps due to the weaker MCAO index anomaly. Over Svalbard, ERA5 displays temperature anomalies of -25 K, which is almost 5 K colder

than in CARRA. The strongest specific humidity anomalies are found near the ice edges, i.e. around 79°N in the north-south cross section and 5°E in the east-west cross section, and reach to around -2.5 g kg^{-1} in both reanalyses. In CARRA, the region of more pronounced humidity anomalies is somewhat more extended towards Svalbard. In contrast to ERA5, CARRA also shows positive humidity anomalies, but these are confined to small regions over the ice in the north and west. The heat flux anomalies are smaller than during the January case, consistent with the weaker MCAO. From the largest values near the ice edge, the heat flux anomalies decrease toward the southeast, likely influenced by the westerly and northwesterly anomalies in the 10 m wind.

6.3 Temporal evolution at a fixed location

As seen in the cross sections, the temperature above Svalbard is heavily impacted by MCAOs. Therefore, we utilize radiosonde-data from Ny-Ålesund to provide a detailed record of the temporal evolution of the troposphere during the two MCAO cases (Figure 11). Ny-Ålesund is located at the southern coast of the Kongsfjord, surrounded by mountains and glaciers, so the lowermost part of the vertical column encounters local orographic effects. With their vertical resolution of ca 5 m (here interpolated to fixed 10 m steps), the radiosonde data can resolve fine structures that are not captured by the reanalyses.

During the January event, the temporal evolution of temperature and humidity in Ny-Ålesund closely matches that of the MCAO index. At the 24th-25th of January, just prior to the onset of the case, Ny-Ålesund experienced near-surface temperatures of around 270 K along with southwesterly winds in the lowest kilometers, and quite strong (18 ms^{-1}) northwesterly winds in the higher troposphere (Figure 11 a). Relatively strong northerly winds are seen through most of the troposphere during the MCAO index peak and on the subsequent day, but thereafter the wind speed declines, as typical according to E. Kolstad (2017). In the lowest 5 km, the coldest conditions are recorded by the 12:00 launch on the 26th, i.e. during the MCAO peak, when the temperature is 249 K near the surface. At this time, several temperature inversions are present. The most pronounced is situated at approximately 5 km height, where the temperature increases 3 K over a couple of hundred meters. In similarity to the temperature, the specific humidity exhibits its highest values on the 25th (Figure 11 c). The driest air is found during the MCAO peak, when the specific humidity is below 0.3 g kg^1 throughout the column. During the subsequent days, the humidity in the lowest kilometer increases to about 1.6 g kg^1, while the humidity variations above 2 kilometers are smaller than 0.5 g kg^1.

As already indicated by Figure 9, the March case is characterized by day-day fluctuations in atmospheric variables (Figure 11 b and d). Northerly winds are quite prevalent, especially in the lower layers. The strongest northerly winds are seen following the highest MCAO index peak on 12th and the second highest peak on the 16th. The temperature and humidity structures are quite complex, but around the time of these peaks, relatively dry and cool conditions prevail in the lowest 5 kilometers. Southwesterly and westerly winds occur, mainly around the onset and the decay of the event, as well as on the 15th. Around the 15th, the temperature and specific humidity in the lower layers also exhibit small peaks, with values around 255 K and 0.8 g kg^1, respectively. Hence, it appears that the westerly winds brought slightly warmer and moister air, despite the MCAO index showing values of 12-13 K, which is classified as a strong to very strong MCAO event according to Papritz and Spengler (2017). Similar to the January case, the near-surface temperature is more than 20 K colder during the MCAO peak than just before the event.

7 Summary and conclusions

We investigated Marine Cold Air Outbreaks (MCAOs) and turbulent surface heat fluxes in Svalbard and Fram Strait using reanalysis data from ERA5 and CARRA, span-

ning November-March 1991-2020. For each reanalysis, we calculated an MCAO index based on the potential temperature difference between the surface and 850 hPa (θ_S-θ_{850}). In addition to a statistical analysis of the atmospheric characteristics associated with MCAOs and their effects on the heat fluxes, we investigated two separate cases using the reanalysis data and radiosonde data from Ny-Ålesund, Svalbard.

We found that the surface sensible heat flux (SSHF) is substantially higher in CARRA than in ERA5, while the surface latent heat flux (SLHF) is somewhat lower. This may indicate that the overestimation (underestimation) of SLHF (SSHF) in ERA5 that has been noted in previous studies is reduced in CARRA, but studies using observation data are needed to confirm this. For SSHF, the difference between ERA5 and CARRA scale with the magnitude of the heat flux, leading to larger differences over ice-free ocean where SSHF is large. When normalizing the differences with the magnitude, the largest difference is found over sea ice, and is three times larger for SLHF than for SSHF. The heat fluxes in both reanalyses show a stronger relation to the MCAO index than WS10, but the latter plays a substantial role for the heat flux variability when the MCAO index is high.

Spatial patterns in the monthly heat flux trends largely mirror the trends in θ_S-θ_{850}. Around most of Svalbard, these trends are positive and reflect declining sea ice. In Fram Strait however, widespread areas of negative trends in the heat fluxes in January are co-located with negative trends in θ_S-θ_{850}, brought about by a larger increase of the potential temperature at 850 hPa than at the surface. In Fram Strait in March, positive θ_S-θ_{850} trends, in turn related to a decrease in the potential temperature at 850 hPa, are to some extent reflected in the positive heat flux trends.

During MCAOs, positive heat flux anomalies are especially pronounced in northern Fram Strait near the ice edge towards the north and west, where the anomalies in θ_S-θ_{850} and wind speed are the largest. In this region, the sensible heat flux in CARRA is roughly doubled during MCAOs, when the flux is 250 W m^{-2} higher than in the extended winter mean. The latent heat flux shows a more moderate increase of 60 W m^{-2}. Cold and dry anomalies are present throughout the troposphere. The specific humidity anomalies tend to be strongest over the ice-free ocean in southern Fram Strait, while the strongest temperature anomalies are found in the vicinity of the ice edge and close to the land surface of Svalbard. In the latter region, the average anomalies during strong MCAOs reach -10 K (-11.5 K) in CARRA (ERA5), while anomalies during individual cases can be more than twice as large. Over ice-free ocean, where the heat fluxes warm the air from below, the strongest temperature anomalies are typically found around 850 hPa rather than at the surface. Although CARRA is warmer than ERA5 in much of the lower troposphere during mean conditions as well as MCAOs, ERA5 is around 0.5 K warmer over the sea ice. In both our MCAO case studies, the near-surface temperature in Ny-Ålesund drops over 20 K from just before the event to the peak in the MCAO index, demonstrating that Svalbard can be heavily impacted by MCAOs. The temperature, humidity and winds are quite variable throughout the troposphere in this topographically complex setting, but cold and dry conditions coincide with the MCAO index peaks.

Appendix A Supplementary figures

Appendix B Open Research

CARRA (Schyberg et al., 2020) data were downloaded from the Copernicus Climate Change Service (C3S) Climate Data Store (CDS). ERA5 (Hersbach et al., 2018, 2017, 2020) data were downloaded from CDS and the MARS catalog. The results contain modified Copernicus Climate Change Service information 2022. Neither the European Commission nor ECMWF is responsible for any use that may be made of the Copernicus information or data it contains. The radiosonde data (Maturilli, 2008, 2020) are available from the PANGEA database.

Acknowledgments

We gratefully acknowledge the funding by the Deutsche Forschungsgemeinschaft (DFG, German Research Foundation) – project no. 268020496 – TRR 172, within the Transregional Collaborative Research Center "ArctiC Amplification: Climate Relevant Atmospheric and SurfaCe Processes, and Feedback Mechanisms $(AC)^3$". We would also like to thank the staff of the AWIPEV research base in Ny-Ålesund for the radiosonde launches contributing to this study.

References

Aagaard, K., & Greisman, P. (1975). Toward new mass and heat budgets for the Arctic Ocean. *Journal of Geophysical Research*, *80*(27), 3821–3827.

Batrak, Y., & Müller, M. (2019). On the warm bias in atmospheric reanalyses induced by the missing snow over Arctic sea-ice. *Nature Communications*, *10*(1), 1–8.

Bengtsson, L., Andrae, U., Aspelien, T., Batrak, Y., Calvo, J., de Rooy, W., ... others (2017). The HARMONIE–AROME model configuration in the ALADIN–HIRLAM NWP system. *Monthly Weather Review*, *145*(5), 1919–1935.

Boisvert, L., Boeke, R., Taylor, P., & Parker, C. (2022). Constraining Arctic climate projections of wintertime warming with surface turbulent flux observations and representation of surface-atmosphere coupling. *Frontiers in Earth Science*, *10*, 765304.

Brümmer, B., & Pohlmann, S. (2000). Wintertime roll and cell convection over Greenland and Barents Sea regions: A climatology. *Journal of Geophysical Research: Atmospheres*, *105*(D12), 15559–15566.

Dahlke, S., & Maturilli, M. (2017). Contribution of atmospheric advection to the amplified winter warming in the Arctic North Atlantic region. *Advances in Meteorology*, *2017*.

Dahlke, S., Solbès, A., & Maturilli, M. (2022). Cold air outbreaks in Fram Strait: climatology, trends, and observations during an extreme season in 2020. *Journal of Geophysical Research: Atmospheres*, *127*(3), e2021JD035741.

ECMWF. (2016). *IFS DOCUMENTATION – Cy41r2. Operational implementation 8 March 2016 PART IV: PHYSICAL PROCESSES.* `https://www.ecmwf.int/sites/default/files/elibrary/2016/16648-part-iv-physical-processes.pdf#section.3.6`. (Online; accessed 15 December 2022)

Fearon, M. G., Doyle, J. D., Ryglicki, D. R., Finocchio, P. M., & Sprenger, M. (2021). The role of cyclones in moisture transport into the Arctic. *Geophysical Research Letters*, *48*(4), e2020GL090353.

Graham, R. M., Cohen, L., Ritzhaupt, N., Segger, B., Graversen, R. G., Rinke, A., ... Hudson, S. R. (2019). Evaluation of six atmospheric reanalyses over Arctic sea ice from winter to early summer. *Journal of Climate*, *32*(14), 4121–4143.

Graham, R. M., Hudson, S. R., & Maturilli, M. (2019). Improved performance of ERA5 in Arctic gateway relative to four global atmospheric reanalyses. *Geophysical Research Letters*, *46*(11), 6138–6147.

Hartmann, J., Kottmeier, C., & Raasch, S. (1997). Roll vortices and boundary-layer development during a cold air outbreak. *Boundary-Layer Meteorology*, *84*(1), 45–65.

Hersbach, H., Bell, B., Berrisford, P., Biavati, G., Horányi, A., Muñoz Sabater, J., ... Thépaut, J.-N. (2018). *ERA5 hourly data on single levels from 1959 to present* [dataset]. Copernicus Climate Change Service (C3S) Climate Data Store (CDS). DOI: 10.24381/cds.adbb2d47.

Hersbach, H., Bell, B., Berrisford, P., Hirahara, S., Horányi, A., Muñoz-Sabater, J., ... others (2020). The ERA5 global reanalysis. *Quarterly Journal of the Royal Meteorological Society*, *146*(730), 1999–2049.

Hersbach, H., Bell, B., Berrisford, P., Hirahara, S., Horányi, A., Muñoz-Sabater, J.,

... Thépaut, J.-N. (2017). *Complete ERA5 from 1979: Fifth generation of ECMWF atmospheric reanalyses of the global climate.* [dataset]. Copernicus Climate Change Service (C3S) Data Store (CDS).

Knudsen, E. M., Heinold, B., Dahlke, S., Bozem, H., Crewell, S., Gorodetskaya, I. V., ... others (2018). Meteorological conditions during the ACLOUD/PASCAL field campaign near Svalbard in early summer 2017. *Atmospheric Chemistry and Physics*, *18*(24), 17995–18022.

Kolstad, E. (2017). Higher ocean wind speeds during marine cold air outbreaks. *QJ Roy. Meteor. Soc.*, *143*, 2084–2092.

Kolstad, E. W. (2011). A global climatology of favourable conditions for polar lows. *Quarterly Journal of the Royal Meteorological Society*, *137*(660), 1749–1761.

Kolstad, E. W., Bracegirdle, T. J., & Seierstad, I. A. (2009). Marine cold-air outbreaks in the North Atlantic: Temporal distribution and associations with large-scale atmospheric circulation. *Climate dynamics*, *33*, 187–197.

Køltzow, M., Schyberg, H., Støylen, E., & Yang, X. (2022). Value of the Copernicus Arctic Regional Reanalysis (CARRA) in representing near-surface temperature and wind speed in the north-east European Arctic. *Polar Research*, *41*.

Martens, B., Schumacher, D. L., Wouters, H., Muñoz-Sabater, J., Verhoest, N. E., & Miralles, D. G. (2020). Evaluating the land-surface energy partitioning in ERA5. *Geoscientific Model Development*, *13*(9), 4159–4181.

Maturilli, M. (2008). *Radiosonde measurements from station Ny-Ålesund (2007-01)* [dataset]. PANGAEA. Retrieved from `https://doi.org/10.1594/PANGAEA.695515` doi: 10.1594/PANGAEA.695515

Maturilli, M. (2020). High resolution radiosonde measurements from station Ny-Ålesund (2020-03) [dataset]. PANGAEA. Retrieved from `https://doi.org/10.1594/PANGAEA.917966` (In: Maturilli, M (2020): High resolution radiosonde measurements from station Ny-Ålesund (2017-04 et seq). Alfred Wegener Institute - Research Unit Potsdam, PANGAEA, https://doi.org/10.1594/PANGAEA.914973) doi: 10.1594/PANGAEA.917966

Maturilli, M., & Kayser, M. (2017). Arctic warming, moisture increase and circulation changes observed in the Ny-Ålesund homogenized radiosonde record. *Theoretical and Applied Climatology*, *130*, 1–17.

Meyer, M., Polkova, I., Modali, K. R., Schaffer, L., Baehr, J., Olbrich, S., & Rautenhaus, M. (2021). Interactive 3-D visual analysis of ERA5 data: improving diagnostic indices for marine cold air outbreaks and polar lows. *Weather and Climate Dynamics*, *2*(3), 867–891.

Michaelis, J., Schmitt, A. U., Lüpkes, C., Hartmann, J., Birnbaum, G., & Vihma, T. (2022). Observations of marine cold-air outbreaks: a comprehensive data set of airborne and dropsonde measurements from the Springtime Atmospheric Boundary Layer Experiment (STABLE). *Earth System Science Data*, *14*(4), 1621–1637.

Nielsen, K. P. and Yang, X. and Agersten, S. and Dahlgren, P. and Ødegaard Køltzow, M. A. and Schyberg, H. and Støylen, E. and Bojarova, J. (2022). *Copernicus Arctic Regional Reanalysis (CARRA): Data User Guide.* `https://confluence.ecmwf.int/display/CKB/Copernicus+Arctic+Regional+Reanalysis+%28CARRA%29%3A+Data+User+Guide`. (Online; accessed 21 December 2022)

Papritz, L., & Spengler, T. (2017). A Lagrangian climatology of wintertime cold air outbreaks in the Irminger and Nordic Seas and their role in shaping air–sea heat fluxes. *Journal of Climate*, *30*(8), 2717–2737.

Pithan, F., Svensson, G., Caballero, R., Chechin, D., Cronin, T. W., Ekman, A. M., ... others (2018). Role of air-mass transformations in exchange between the Arctic and mid-latitudes. *Nature Geoscience*, *11*(11), 805–812.

Polkova, I., Afargan-Gerstman, H., Domeisen, D. I., King, M. P., Ruggieri, P., Athanasiadis, P., ... Baehr, J. (2021). Predictors and prediction skill for

marine cold-air outbreaks over the Barents Sea. *Quarterly Journal of the Royal Meteorological Society*, *147*(738), 2638–2656.

Renfrew, I. A., Barrell, C., Elvidge, A., Brooke, J., Duscha, C., King, J., ... others (2021). An evaluation of surface meteorology and fluxes over the Iceland and Greenland Seas in ERA5 reanalysis: The impact of sea ice distribution. *Quarterly Journal of the Royal Meteorological Society*, *147*(734), 691–712.

Rudels, B., Korhonen, M., Budéus, G., Beszczynska-Möller, A., Schauer, U., Nummelin, A., ... Valdimarsson, H. (2012). The East Greenland Current and its impacts on the Nordic Seas: observed trends in the past decade. *ICES Journal of Marine Science*, *69*(5), 841–851.

Schyberg, H., Yang, X., Køltzow, M., Amstrup, B., Bakketun, Å., Bazile, E., ... Wang, Z. (2020). *Arctic regional reanalysis on single levels from 1991 to present.* [dataset]. `https://cds.climate.copernicus.eu/cdsapp#!/dataset/reanalysis-carra-single-levels?tab=overview`.

Strong, C., Foster, D., Cherkaev, E., Eisenman, I., & Golden, K. M. (2017). On the definition of marginal ice zone width. *Journal of Atmospheric and Oceanic Technology*, *34*(7), 1565–1584.

Taylor, P. C., Hegyi, B. M., Boeke, R. C., & Boisvert, L. N. (2018). On the increasing importance of air-sea exchanges in a thawing Arctic: A review. *Atmosphere*, *9*(2), 41.

Terpstra, A., Renfrew, I. A., & Sergeev, D. E. (2021). Characteristics of cold-air outbreak events and associated polar mesoscale cyclogenesis over the North Atlantic region. *Journal of Climate*, *34*(11), 4567–4584.

Tsukernik, M., Kindig, D. N., & Serreze, M. C. (2007). Characteristics of winter cyclone activity in the northern North Atlantic: Insights from observations and regional modeling. *Journal of Geophysical Research: Atmospheres*, *112*(D3).

Wang, C., Graham, R. M., Wang, K., Gerland, S., & Granskog, M. A. (2019). Comparison of ERA5 and ERA-Interim near-surface air temperature, snowfall and precipitation over Arctic sea ice: effects on sea ice thermodynamics and evolution. *The Cryosphere*, *13*(6), 1661–1679.

Wickström, S., Jonassen, M., Vihma, T., & Uotila, P. (2020). Trends in cyclones in the high-latitude North Atlantic during 1979–2016. *Quarterly Journal of the Royal Meteorological Society*, *146*(727), 762–779.

Yang, X., Schyberg, H., Palmason, B., Bojarova, J., Box, J., Pagh Nielsen, K., ... Mankoff, K. (2020). *C3S Arctic regional reanalysis—full system documentation.* `https://datastore.copernicus-climate.eu/documents/reanalysis-carra/CARRAFullSystemDocumentationFinal.pdf`.

Figure 1. Daily mean CARRA vs ERA5 surface heat fluxes in the Fram Strait, November-March 1991-2020. Points over ice-free ocean (dark crosses), the Marginal Ice Zone (MIZ; blue dots) and sea ice (bright stars) are shown for surface sensible heat flux (SSHF; a) and surface latent heat flux (SLHF; b).

Figure 2. Daily mean 10 m wind speed (WS10) and surface heat fluxes for different Marine Cold Air Outbreak (MCAO) index strengths (color-coded), for surface sensible heat flux (SSHF; a & c) and surface latent heat flux (SLHF; b & d) from CARRA (a & b) and ERA5 (c & d). WS10 in CARRA and ERA5 is shown in (e) as boxplots (where the black line in each box marks the median, the bottom (top) marks the 25th (75th) percentile and the whiskers extend to the most extreme value not considered an outlier, with outliers plotted as circles and defined as values > 1.5 times the interquartile range outside the box).

Figure 3. Monthly mean trends in CARRA over the 1991-2020 period, for January (top row) and March (bottom row), for the surface-atmosphere potential temperature difference (θ_S-θ_{850}; a & e), surface sensible heat flux (SSHF; b & f), surface latent heat flux (SLHF; c & g) and sea ice concentration (SIC; d & h). Dotting denotes regions where the trend is not statistically significant. In subplot (h), the black box shows the extent

of the Fram Strait for which the Marine Cold Air Outbreak (MCAO) index was calculated, the red cross shows the location of the radiosonde launch site in Ny-Ålesund, and the two black lines show the cross sections at 6°E and 79°N, respectively.

Figure 4. CARRA surface fluxes, surface-atmosphere potential temperature difference (θ_S-θ_{850}), sea surface temperature (SST) and 10 m wind, for November-March 1991-2020. Mean conditions (left column) and Marine Cold Air Outbreak (MCAO) anomalies (right column) are shown for surface sensible heat flux (SSHF; a & e), surface latent heat flux (SLHF; b & f), θ_S-θ_{850} (c & g), SST (contour lines in c & g), and 10 m wind speed and direction (d & h; the colors show the scalar average speed, the arrows show direction and vector average speed).

Figure 5. Cross sections at 6°E (vertical line in Figure 3 h), from the surface to 300 hPa, showing temperature (colors), specific humidity (contour lines) and wind (barbs), for November-March 1991-2020. Mean conditions are shown in the left column and Marine Cold Air Outbreak (MCAO) anomalies are shown in the right column, for CARRA (top) and CARRA-ERA5 (bottom). Vertical lines (in a-b) denote transitions between regions dominated by sea ice or ocean (ICE and SEA, respectively), for mean conditions (solid) and MCAO conditions (dashed).

Figure 6. Cross sections at 79°N (horizontal line in Figure 3 h), from the surface to 300 hPa, showing temperature (colors), specific humidity (contour lines) and wind (barbs), for November-March 1991-2020. Mean conditions are shown in the left column and Marine Cold Air Outbreak (MCAO) anomalies are shown in the right column, for CARRA (top) and CARRA-ERA5 (bottom). Vertical lines denote transitions between regions dominated by sea ice, ocean or land (ICE, SEA and SVA, respectively), for mean conditions (solid) and MCAO conditions (dashed).

Figure 7. CARRA (darker shades) and ERA5 (lighter shades) 3-hourly Marine Cold Air Outbreak (MCAO) index, surface sensible heat flux (SSHF), surface latent heat flux (SLHF) and 10 m wind speed (WS10) during an MCAO event in January 2007. The data were averaged over the ice-free fraction of the Fram Strait.

Figure 8. Temperature, wind, specific humidity and heat flux anomalies for the Marine Cold Air Outbreak (MCAO) case in January 2007. The anomalies are calculated as the daily mean of the 26th-the daily mean of the 24th. Cross sections at 6°E (a & c) and 79°N (b & d) are shown for CARRA (left) and ERA5 (right), along with surface sensible heat flux (SSHF; dash-dotted line, right y-axis) and surface latent heat flux (SLHF; dashed line, right y-axis). Thin vertical solid (dashed) lines show the transitions between sea ice (ICE), land (SVA) and ocean (SEA) on the 26th (24th) while the thicker, white vertical line in subplots (b) and (d) indicate the location of the radiosonde launch site. CARRA SSHF and SLHF are shown in (e) & (f), respectively, and ERA5 SSHF and SLHF are shown in (g) & (h), respectively.

Figure 9. CARRA (darker shades) and ERA5 (lighter shades) 3-hourly Marine Cold Air Outbreak (MCAO) index, surface sensible heat flux (SSHF), surface latent heat flux (SLHF) and 10 m wind speed (WS10) during an MCAO event in March 2020. The data were averaged over the ice-free fraction of the Fram Strait.

Figure 10. Temperature, wind, specific humidity and heat flux anomalies for the Marine Cold Air Outbreak (MCAO) case in March 2020. The anomalies are calculated as the daily mean of the 12th-the daily mean of the 5th. Cross sections at 6°E (a & c) and 79°N (b & d) are shown for CARRA (left) and ERA5 (right), along with surface sensible heat flux (SSHF; dash-dotted line, right y-axis) and surface latent heat flux (SLHF; dashed line, right y-axis). Thin vertical solid (dashed) lines show the transitions between sea ice (ICE), land (SVA) and ocean (SEA) on the 12th (5th) while the thicker, white vertical line in subplots (b) and (d) indicate the location of the radiosonde launch site. CARRA SSHF and SLHF are shown in (e) & (f), respectively, and ERA5 SSHF and SLHF are shown in (g) & (h), respectively.

Figure 11. Ny-Ålesund radiosonde data for the Marine Cold Air Outbreak (MCAO) cases in January 2007 (a & c) and March 2020 (b & d). Air temperature is shown along

with wind barbs and the 3-hourly MCAO indices from CARRA (black, right y-axis) and ERA5 (grey, right y-axis) in (a) and (b). Specific humidity is shown in (c) and (d).

Figure A1. Monthly mean 1991-2020 MCAO indices for CARRA (black, left y-axis) and ERA5 (grey, left y-axis) are plotted along with surface sensible heat flux (dash-dot, right y-axis) and surface latent heat flux (dotted, right y-axis), with the numbers a-e representing the months November to March. For the fluxes, the dark purple represents CARRA and the light green represents ERA5. The trends are given in the box to the right in each subplot. All data were averaged over the ice-free part of Fram Strait.

Figure A2. Monthly mean trends in ERA5 over the 1991-2020 period, for January (top row) and March (bottom row), for the surface-atmosphere potential temperature difference (θ_S-θ_{850}; a & e), surface sensible heat flux (SSHF; b & f), surface latent heat flux (SLHF; c & g) and sea ice concentration (SIC; d & h). Dotting denotes regions where the trend is not statistically significant.

Figure A3. ERA5 surface fluxes, surface-atmosphere potential temperature difference (θ_S-θ_{850}), sea surface temperature (SST) and 10 m wind, for November-March 1991-2020. Mean conditions (left column) and Marine Cold Air Outbreak (MCAO) anomalies (right column) are shown for surface sensible heat flux (SSHF; a & e), surface latent heat flux (SLHF; b & f), θ_S-θ_{850} (c & g), SST (contour lines in c & g), and 10 m wind speed and direction (d & h; the colors show the scalar average speed, the arrows show direction and vector average speed).

Figure01.

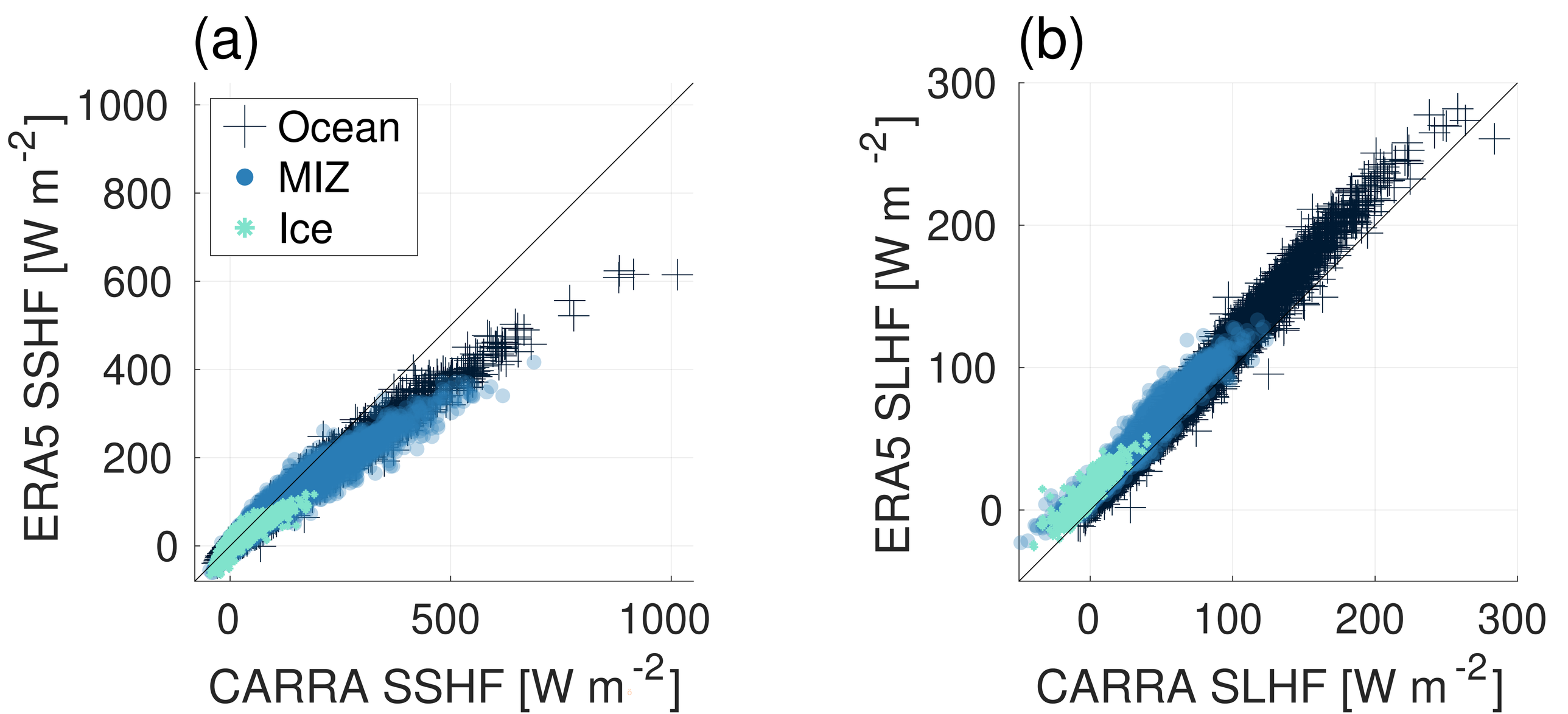
(a)
Ocean
MIZ
Ice
ERA5 SSHF [W m-2]
CARRA SSHF [W m-2]
0
200
400
600
800
1000
0
500
1000
(b)
ERA5 SLHF [W m-2]
CARRA SLHF [W m-2]
0
100
200
300
0
100
200
300

Figure02.

(a)

CARRA

SSHF [W m^{-2}]

WS10 [m s^{-1}]

(b)

CARRA

SLHF [W m^{-2}]

WS10 [m s^{-1}]

MCAO ≤-6
-6< MCAO ≤-4
-4< MCAO ≤-2
-2< MCAO ≤0
0< MCAO ≤2
2< MCAO ≤4
4< MCAO ≤6
6< MCAO ≤8
8< MCAO ≤10
10< MCAO ≤12
12< MCAO

(c)

ERA5

SSHF [W m^{-2}]

WS10 [m s^{-1}]

(d)

ERA5

SLHF [W m^{-2}]

WS10 [m s^{-1}]

(e)

WS10 [m s^{-1}]

CARRA

ERA5

Figure03.

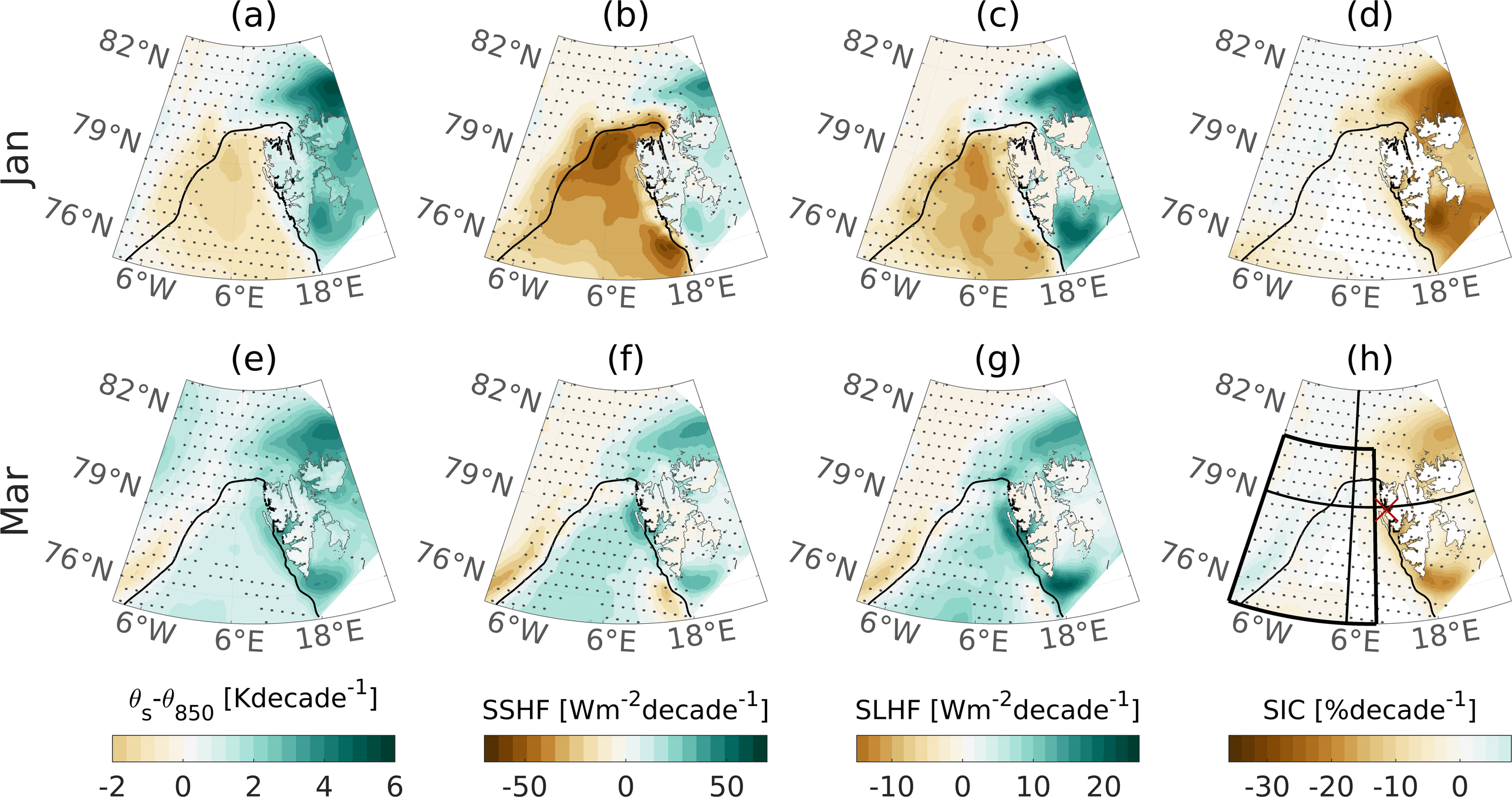
(a)
(b)
(c)
(d)
(e)
(f)
(g)
(h)
Jan
Mar
82°N
79°N
76°N
6°W
6°E
18°E
θ_s-θ_{850} [Kdecade^{-1}]
-2 0 2 4 6
SSHF [Wm^{-2}decade^{-1}]
-50 0 50
SLHF [Wm^{-2}decade^{-1}]
-10 0 10 20
SIC [%decade^{-1}]
-30 -20 -10 0

Figure04.

(a)

SSHF [W m^{-2}]

200

100

0

-100

82°N

79°N

76°N

6°W

6°E

18°E

(e)

SSHF [W m^{-2}]

200

100

0

-100

82°N

79°N

76°N

6°W

6°E

18°E

(b)

SLHF [W m^{-2}]

100

50

0

82°N

79°N

76°N

6°W

6°E

18°E

(f)

SLHF [W m^{-2}]

100

50

0

82°N

79°N

76°N

6°W

6°E

18°E

SST [K]

279

278

277

276

275

274

273

272

(c)

θ_{sk}-θ_{850} [K]

5

0

-5

-10

-15

82°N

79°N

76°N

6°W

6°E

18°E

(g)

θ_{sk}-θ_{850} [K]

8

6

4

2

0

-2

82°N

79°N

76°N

6°W

6°E

18°E

SST [K]

0

-0.1

-0.2

-0.3

-0.4

-0.5

(d)

WS10 [m s^{-1}]

5 m/s

9

8

7

6

5

82°N

79°N

76°N

6°W

6°E

18°E

(h)

WS10 [m s^{-1}]

4

2

0

-2

-4

82°N

79°N

76°N

6°W

6°E

18°E

Figure05.

Temperature [K]

220 230 240 250 260 270

Wind speed [m×s^{-1}]

15.4
12.9
10.3
7.7
5.1
2.6
<2.6

(a): CARRA MEAN

(c): CARRA MCAO

Temperature [K]

-10 -8 -6 -4 -2 0

Pressure level [hPa]

(b): CARRA-ERA5 MEAN

(d): CARRA-ERA5 MCAO

Specific humidity

q [g kg^{-1}]

Latitude

Temperature [K]

-0.5 0 0.5

Figure06.

Temperature [K]

220 230 240 250 260 270

Wind speed [m×s^{-1}]

15.4
12.9
10.3
7.7
5.1
2.6
<2.6

(a): CARRA MEAN

ICE SEA SVA. ICE

0.2 0.4 0.6 0.3 1 1.2 1.4 1.6 1 0.2 0.4 0.6 0.8 1 1.2 1.2

Pressure level [hPa]

300 400 500 600 700 800 900 1000

0 10 20

Temperature [K]

-10 -8 -6 -4 -2 0

(c): CARRA MCAO

ICE SEA SVA. ICE

-0.1 -0.2 -0.3 -0.4 -0.5 -0.6 -0.7 -0.5 -0.6 -0.7 -0.8 -0.1 -0.2 -0.3 -0.4 -0.5 -0.6

300 400 500 600 700 800 900 1000

0 10 20

(b): CARRA-ERA5 MEAN

0.05 0.05 0.05 0.05 0.05 0.05 0.05 -0.02

600 650 700 750 800 850 900 950 1000

0 10 20

(d): CARRA-ERA5 MCAO

Specific humidity

q [g kg^{-1}]

0.05 0.005 0.005 0.005 0.005 0.005

600 650 700 750 800 850 900 950 1000

0 10 20

Longitude

Temperature [K]

-1.5 -1 -0.5 0 0.5 1 1.5

Temperature [K]

-1.5 -1 -0.5 0 0.5 1 1.5

Figure07.

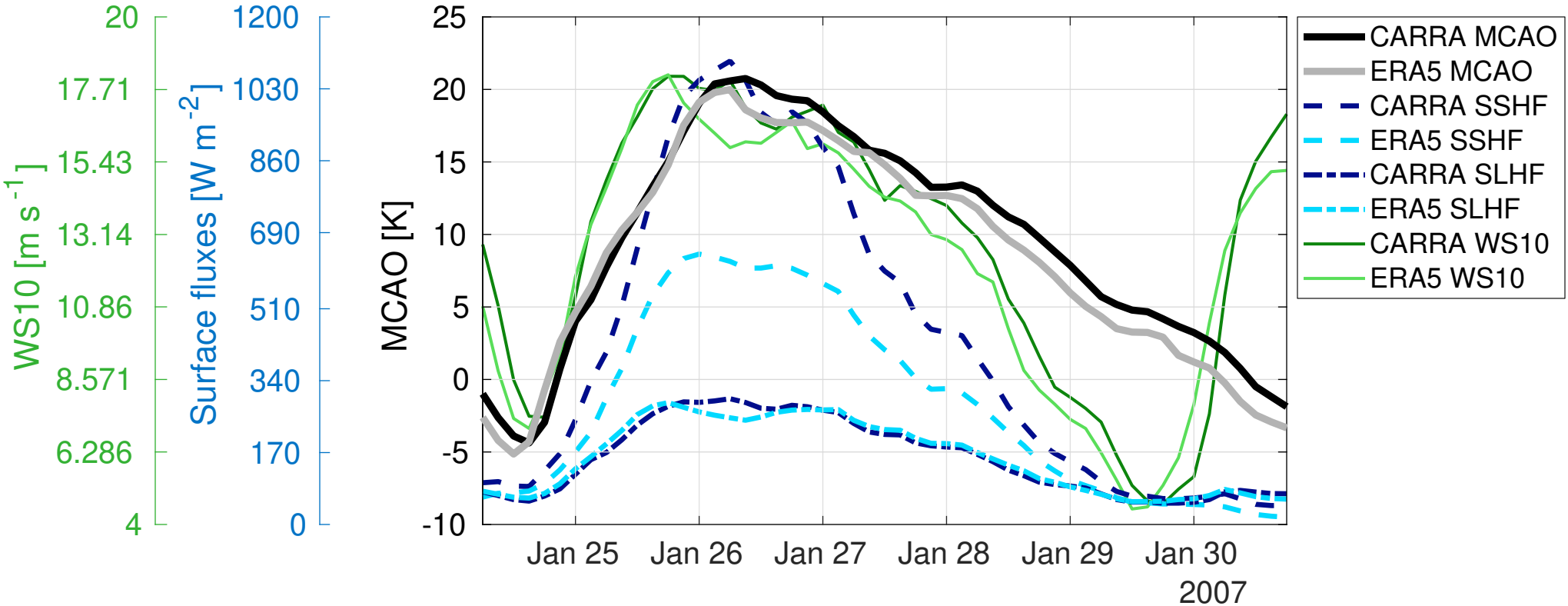
WS10 [m s-1]
Surface fluxes [W m-2]
MCAO [K]
20
17.71
15.43
13.14
10.86
8.571
6.286
4
1200
1030
860
690
510
340
170
0
25
20
15
10
5
0
-5
-10
Jan 25
Jan 26
Jan 27
Jan 28
Jan 29
Jan 30
2007
CARRA MCAO
ERA5 MCAO
CARRA SSHF
ERA5 SSHF
CARRA SLHF
ERA5 SLHF
CARRA WS10
ERA5 WS10

Figure08.

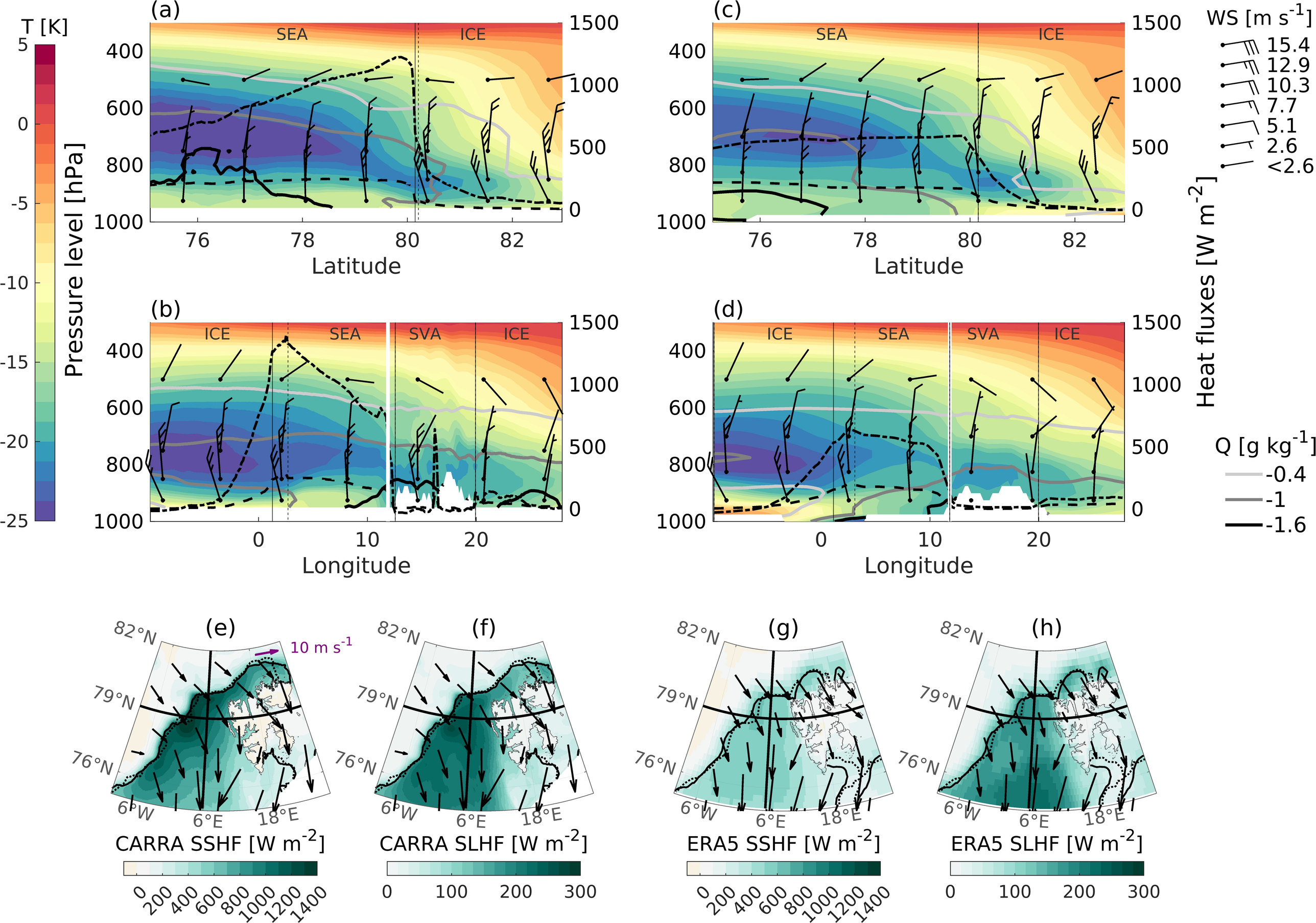
T [K]
5
0
-5
-10
-15
-20
-25
Pressure level [hPa]
(a)
(b)
(c)
(d)
SEA
ICE
SVA
400
600
800
1000
1500
1000
500
0
76
78
80
82
Latitude
0
10
20
Longitude
WS [m s-1]
15.4
12.9
10.3
7.7
5.1
2.6
<2.6
Heat fluxes [W m-2]
Q [g kg-1]
-0.4
-1
-1.6
(e)
(f)
(g)
(h)
82°N
79°N
76°N
6°W
6°E
18°E
10 m s-1
CARRA SSHF [W m-2]
CARRA SLHF [W m-2]
ERA5 SSHF [W m-2]
ERA5 SLHF [W m-2]
0
200
400
600
800
1000
1200
1400
100
300

Figure09.

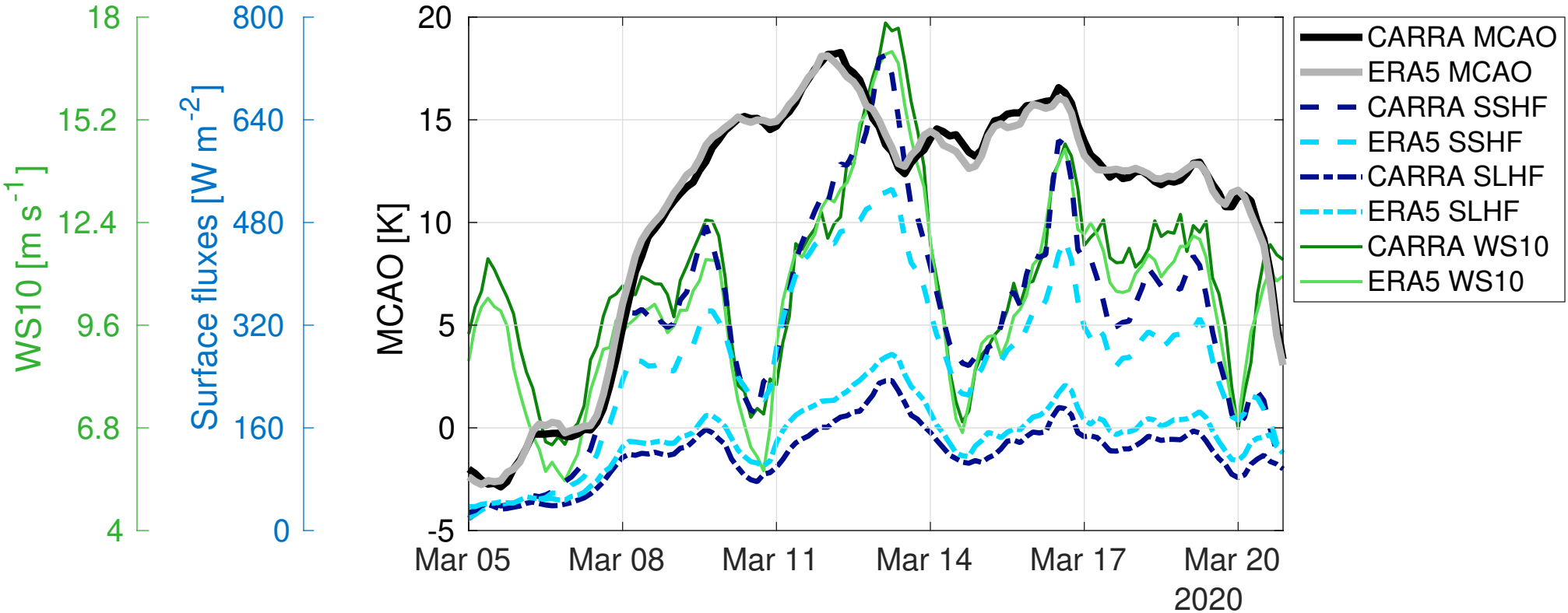
WS10 [m s-1]
Surface fluxes [W m-2]
MCAO [K]
18
15.2
12.4
9.6
6.8
4
800
640
480
320
160
0
20
15
10
5
0
-5
Mar 05
Mar 08
Mar 11
Mar 14
Mar 17
Mar 20
2020
CARRA MCAO
ERA5 MCAO
CARRA SSHF
ERA5 SSHF
CARRA SLHF
ERA5 SLHF
CARRA WS10
ERA5 WS10

Figure10.

T [K]
5
0
-5
-10
-15
-20
-25

(a)
(b)
(c)
(d)
SEA
ICE
SVA
Pressure level [hPa]
400
600
800
1000
500
0
76
78
80
82
Latitude
0
10
20
Longitude

WS [m s^{-1}]
15.4
12.9
10.3
7.7
5.1
2.6
<2.6

Heat fluxes [W m^{-2}]

Q [g kg^{-1}]
0.4
-0.2
-0.8
-1.4
-2

(e)
(f)
(g)
(h)
82°N
79°N
76°N
6°W
6°E
18°E
10 m s^{-1}
CARRA SSHF [W m^{-2}]
CARRA SLHF [W m^{-2}]
ERA5 SSHF [W m^{-2}]
ERA5 SLHF [W m^{-2}]
-200
0
200
400
600
800
-100
0
100
200

Figure11.

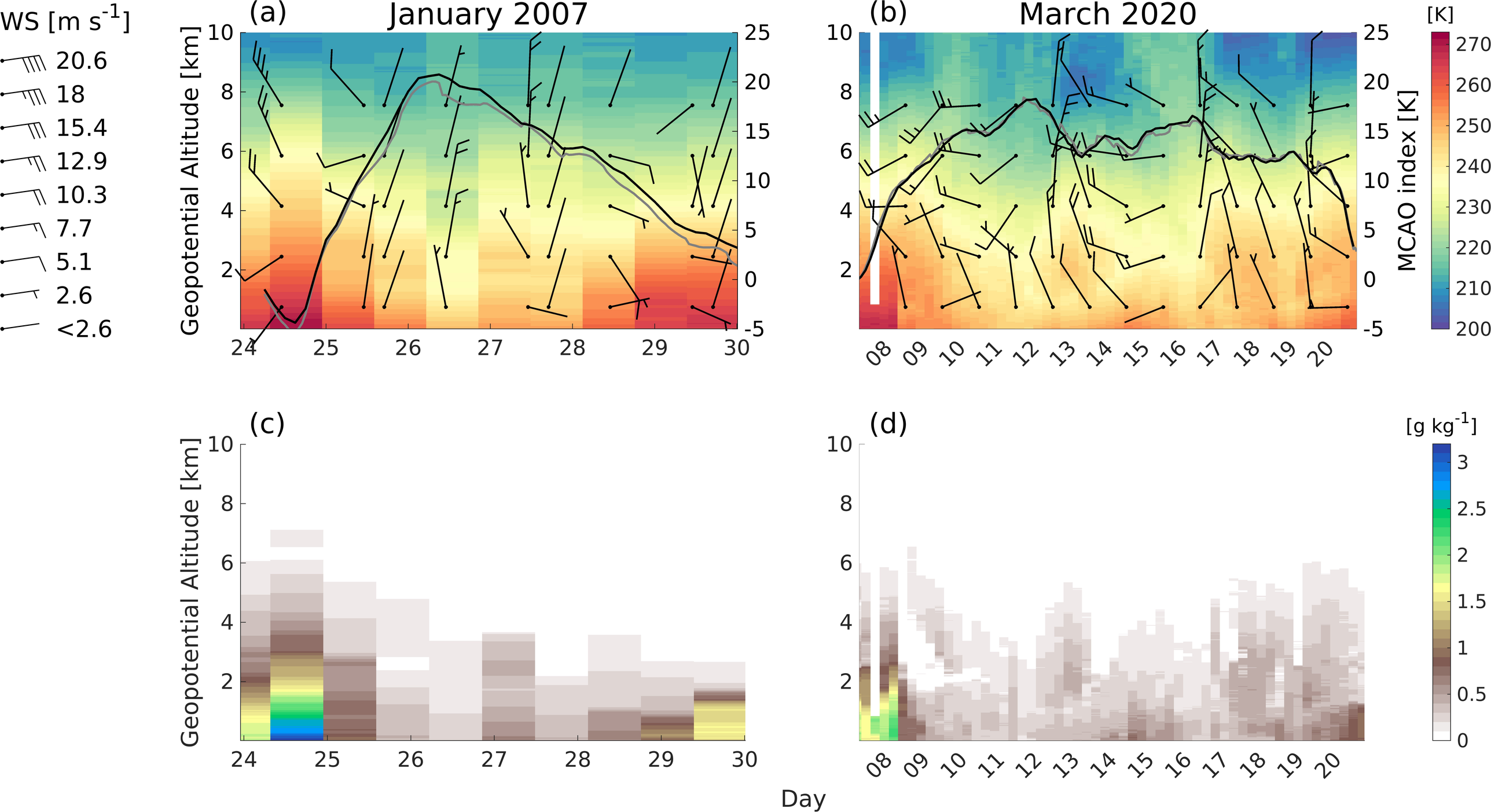
WS [m s-1]
20.6
18
15.4
12.9
10.3
7.7
5.1
2.6
<2.6
(a)
January 2007
(b)
March 2020
Geopotential Altitude [km]
MCAO index [K]
[K]
(c)
(d)
[g kg-1]
Day

_appendixFigure01.

(a)


Nov
10
5
0
-5
1995
2000
2005
2010
2015
2020
250
200
150
100
50
Decadal Trends
-0.1
0
-2.7
0.8
1.2
2.6

(b)

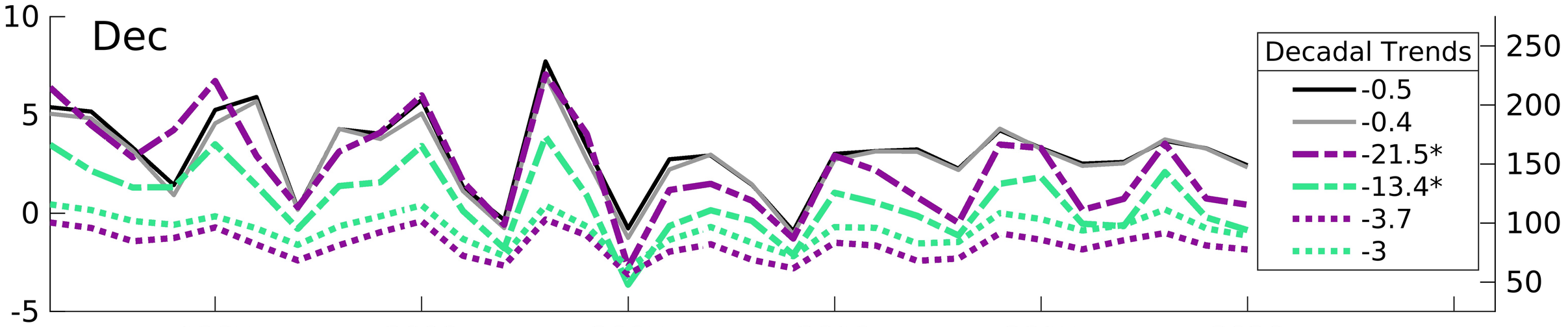
Dec
10
5
0
-5
1995
2000
2005
2010
2015
2020
250
200
150
100
50
Decadal Trends
-0.5
-0.4
-21.5*
-13.4*
-3.7
-3

(c)

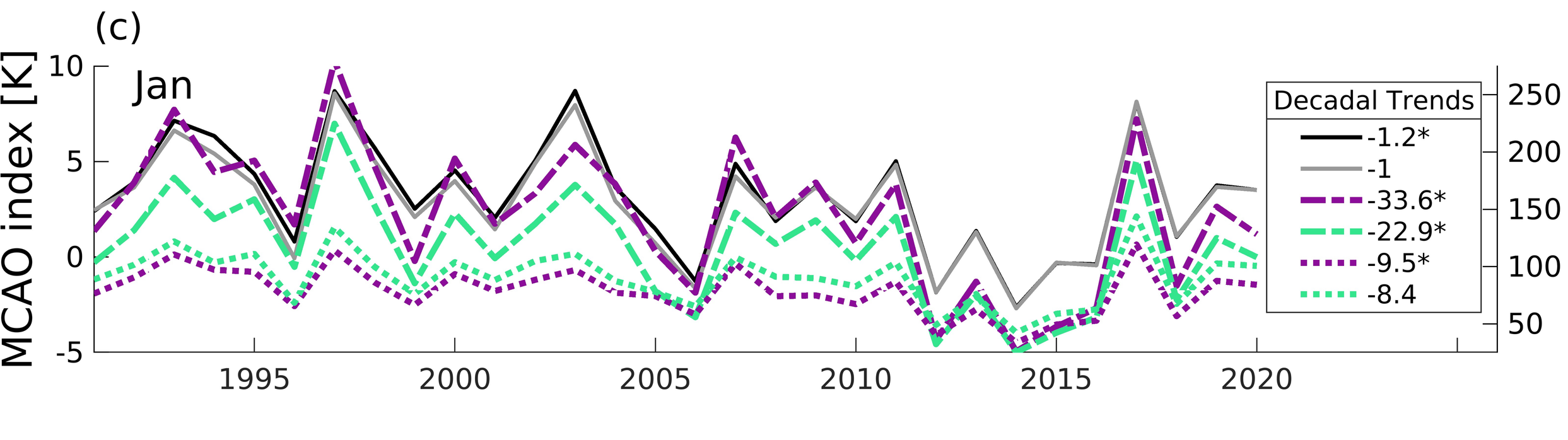
Jan
10
5
0
-5
1995
2000
2005
2010
2015
2020
250
200
150
100
50
Decadal Trends
-1.2*
-1
-33.6*
-22.9*
-9.5*
-8.4
MCAO index [K]
Surface fluxes [W m-2]

(d)

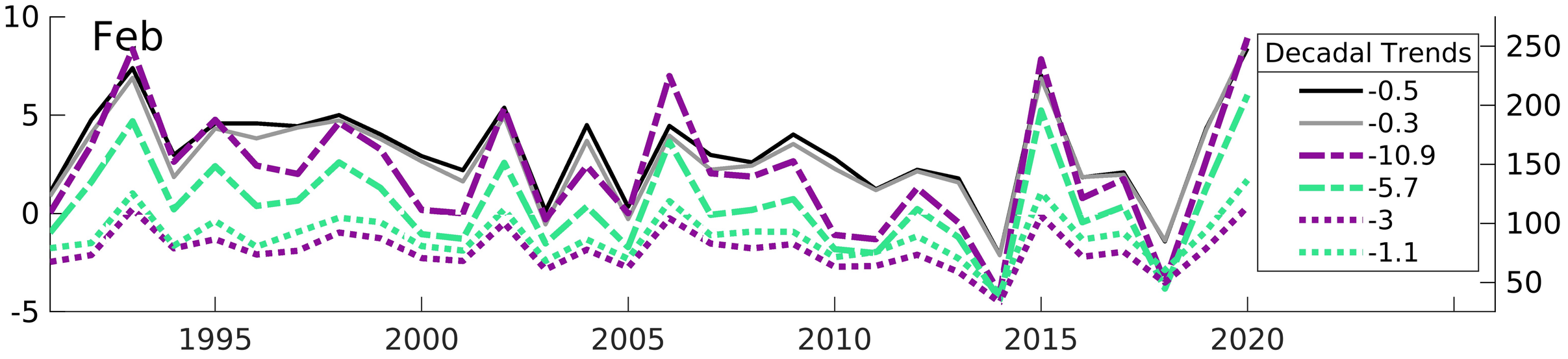
Feb
10
5
0
-5
1995
2000
2005
2010
2015
2020
250
200
150
100
50
Decadal Trends
-0.5
-0.3
-10.9
-5.7
-3
-1.1

(e)

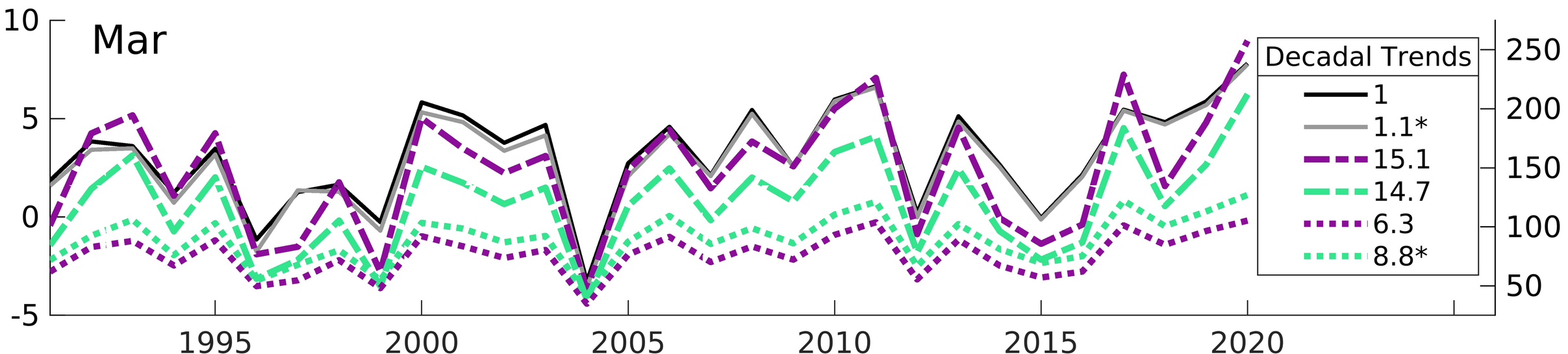
Mar
10
5
0
-5
1995
2000
2005
2010
2015
2020
250
200
150
100
50
Decadal Trends
1
1.1*
15.1
14.7
6.3
8.8*

_appendixFigure02.

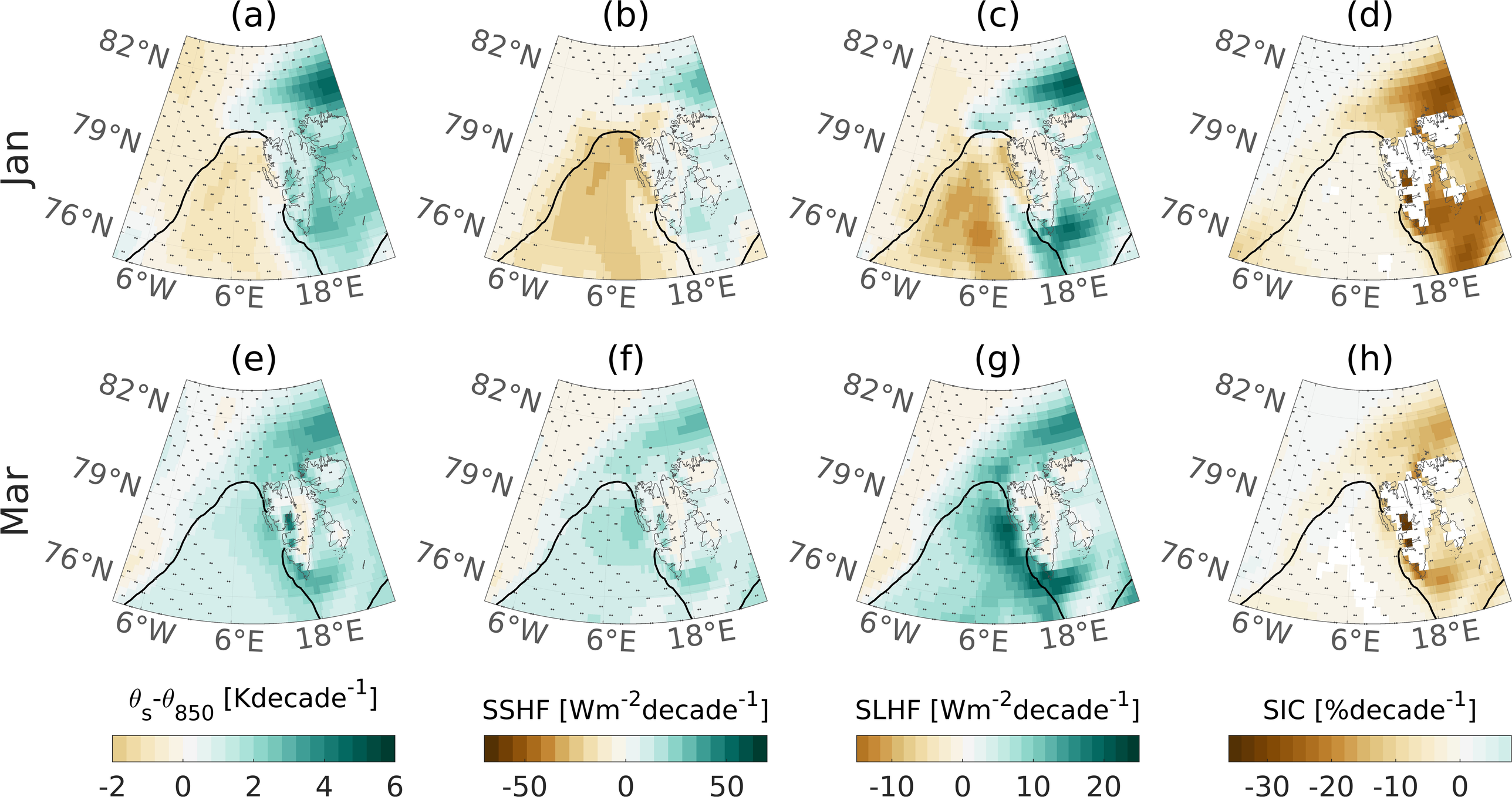
(a)
(b)
(c)
(d)
(e)
(f)
(g)
(h)
Jan
Mar
82°N
79°N
76°N
6°W
6°E
18°E
θ_s-θ_{850} [Kdecade^{-1}]
-2
0
2
4
6
SSHF [Wm^{-2}decade^{-1}]
-50
0
50
SLHF [Wm^{-2}decade^{-1}]
-10
0
10
20
SIC [%decade^{-1}]
-30
-20
-10
0

Figure_appendixFigure03.

(a)

SSHF [W m^{-2}]

200

100

0

-100

82°N

79°N

76°N

6°W

6°E

18°E

(e)

SSHF [W m^{-2}]

200

100

0

-100

82°N

79°N

76°N

6°W

6°E

18°E

(b)

SLHF [W m^{-2}]

100

50

0

82°N

79°N

76°N

6°W

6°E

18°E

(f)

SLHF [W m^{-2}]

100

50

0

82°N

79°N

76°N

6°W

6°E

18°E

SST [K]

279

278

277

276

275

274

273

272

(c)

θ_{sk}-θ_{850} [K]

5

0

-5

-10

-15

82°N

79°N

76°N

6°W

6°E

18°E

(g)

θ_{sk}-θ_{850} [K]

8

6

4

2

0

-2

82°N

79°N

76°N

6°W

6°E

18°E

SST [K]

0

-0.1

-0.2

-0.3

-0.4

-0.5

(d)

WS10 [m s^{-1}]

5 m/s

9

8

7

6

5

82°N

79°N

76°N

6°W

6°E

18°E

(h)

WS10 [m s^{-1}]

4

2

0

-2

-4

82°N

79°N

76°N

6°W

6°E

18°E